# Suppressing DNMT3a Alleviates the Intrinsic Epigenetic Barrier for Optic Nerve Regeneration and Restores Vision in Adult Mice

Wai Lydia Tai[1], Kin-Sang Cho[1], Emil Kriukov[1], Ajay Ashok[1], Xuejian Wang[1,2], Aboozar Monavarfeshani[3], Wenjun Yan[3], Yingqian Li[1], Timothy Guan[1], Joshua R. Sanes[3], Petr Baranov[1], Dong Feng Chen[1*]

[1]Schepens Eye Research Institute of Mass Eye and Ear, Department of Ophthalmology, Harvard Medical School, Boston, MA, USA. [2]School of Pharmacy, Weifang Medical University, Weifang, Shandong, China. [3]Department of Cellular and Molecular Biology, Center for Brain Science, Harvard University, MA, USA.

Corresponding author: Dongfeng_chen@meei.harvard.edu

**ABSTRACT**

The limited regenerative potential of the optic nerve in adult mammals presents a major challenge for restoring vision after optic nerve trauma or disease. The mechanisms of this regenerative failure are not fully understood[1,2]. Here, through small-molecule and genetic screening for epigenetic modulators[3], we identify DNA methyltransferase 3a (DNMT3a) as a potent inhibitor of axon regeneration in mouse and human retinal explants. Selective suppression of DNMT3a in retinal ganglion cells (RGCs) by gene targeting or delivery of shRNA leads to robust, full-length regeneration of RGC axons through the optic nerve and restoration of vision in adult mice after nerve crush injury. Genome-wide bisulfite and transcriptome profiling in combination with single nucleus RNA-sequencing of RGCs revealed selective DNA demethylation and reactivation of genetic programs supporting neuronal survival and axonal growth/regeneration by DNMT3a deficiency. This was accompanied by the suppression of gene networks associated with apoptosis and inflammation. Our results identify DNMT3a as the central orchestrator of an RGC-intrinsic mechanism that limits optic nerve regeneration. Suppressing DNMT3a expression in RGCs unlocks the epigenetic switch for optic nerve regeneration and presents a promising therapeutic avenue for effectively reversing vision loss resulted from optic nerve trauma or diseases.

**MAIN TEXT**

Mature neurons in the central nervous system (CNS) of adult mammals regenerate poorly after injury. Tremendous efforts have been devoted to study the cellular and molecular origins of this regenerative failure, yet no treatment exists for successful stimulation of CNS regeneration in humans. Eye-to-brain circuits, consisting of retinal ganglion cells (RGCs) whose axons form the optic nerve and connect to the central target areas, is an attractive model system for investigation of factors that regulate CNS axon regeneration because of their accessibility and simple anatomy. However, despite decades of research, achieving functional regeneration of the optic nerve has proved to be an elusive goal. Optic nerve regeneration requires a complex sequence of steps controlled by intricate gene networks that mediate crucial processes such as RGC survival, axonal elongation and guidance, and reformation of synapsis and neural circuitry[1,4]. The current prevailing view is that functional regeneration of the optic nerve cannot be achieved by the activation of a single gene or transcription factor[1,2], but rather requires modulation of multiple gene expression or programs.

Embryonic RGCs possess the innate ability to regenerate optic nerve fibers and readily grow their axons even when presented with a hostile or adult brain environment (growth-inhibitory)[5,6]. However, this ability of RGCs is lost perinatally[4-7] at a time coinciding with dynamic changes in epigenetic factors during RGC maturation[8]. We hypothesized that RGC axon growth programs are switched off during maturation through an epigenetic silencing mechanism involving DNA methylation. Indeed, a recent study demonstrated promising results in reprogramming the epigenomes of adult RGCs through the ectopic expression of three transcription factors used to generate stem cells – Oct4, Sox2, and Klf4 (Yamanaka factors)[9]. This resulted in partial restoration of youthful DNA methylation patterns and significant axon regeneration following crush injury. To date, however, no known strategy fully restores optic nerve regeneration with visual recovery following nerve injury in adult mammals. We sought strategies to unleash and completely reverse the epigenetic blockade and restore the regenerative potential of the optic nerve in adult mammals. We show here that DNMT3a is pivotal for postnatal onset of optic nerve regenerative failure, and suppression of this single gene results in reprogramming of RGC transcriptomic landscape to enable unprecedented level of optic nerve regeneration and reversal of vision loss in adult mice.

**RGC axon growth enabled by *Dnmt3a* deficiency**

Mouse RGCs lose their intrinsic ability to regenerate axons around embryonic day 18 (E18), one day before birth (postnatal day 0; P0)[5]. To assess epigenetic mechanisms responsible for this decline, we examined the expression patterns of DNA methyltransferases (DNMTs) in developing RGCs of mouse pups aged E16, P0, and P10, which is, before, at, and after the time that RGCs lose their ability to regenerate axons. Quantitative polymerase chain reaction (qPCR) of purified RGCs showed that the expression of *Dnmt3a* increased significantly from E16 to P10, which corresponded to the decline of RGCs' axon regenerative capacity (**Fig. 1a**). Other DNMTs, including *Dnmt1* and *Dnmt3b*, did not exhibit this correlation (**Extended Data Fig. 1a**). Immunohistochemistry confirmed this result: expression of DNMT3a was absent in E16 RGCs or retina but intense in P10 retina (**Fig. 1b** and **Extended Data Fig. 1b**), which was especially pronounced in the RGCs as evident by colocalization with RBPMS, an RGC marker (**Fig. 1b**). Moreover, *Dnmt3a* levels were increased in the RGCs two days after optic nerve crush injury (ONC; **Fig. 1c**), while *Dnmt1* and *Dnmt3b* remained unchanged or downregulated (**Extended Data Fig. 1c**). These data suggest a correlation between DNMT3a upregulation and the decrease of optic nerve regenerative capacity in mice.

To ascertain whether DNMTs affect RGC axonal regrowth, we assessed the effects of decitabine, a commercially available pan DNMT inhibitor[10] *in vitro.* The antagonistic effect of decitabine on DNMTs in post-mitotic neurons in the retina and brain of adult mice has been well documented[11-13]. We thus applied decitabine to retinal explant cultures, where the growth of axons mirrors the regenerative capacity of axotomized optic nerve fibers *in vivo*[5,6]. Consistent with the lack of nerve regeneration, retinal explants of adult (> 2 months old) wildtype mice and post-mortem human eyes showed minimal axonal outgrowth as revealed by β-III tubulin immunolabeling. In contrast, both mouse and human retinal explants treated with decitabine exhibited significant increases in the number and length of axonal growth (**Fig. 1d-j**).

We next adopted a genetic approach to determine which DNMT(s) regulate axon growth capacity in postnatal RGCs. Two DNMT families play different roles in methylation: DNMT1 maintains the methylation patterns, whereas the DNMT3 family (especially DNMT3a and DNMT3b) establishes initial methylation patterns[14]. We generated conditional knockout mice carrying RGC-specific allele with abolished catalytic activity of *Dnmt1* ($CKO^{Dnmt1}$)[15] or *Dnmt3a* ($CKO^{Dnmt3a}$)[16]. *Vglut2-Cre* transgenic mice were previously shown to drive expression of *Cre* recombinase in virtually all RGCs and sporadically cone photoreceptors, but not other retinal cell types[17,18]. We verified this by crossing *Vglut2-Cre* transgenic mice with the *Ai9* mouse line, which expresses the fluorescent reporter tdTomato from the Rosa26 locus in a *Cre*-dependent manner (*R26-tdTomato*). Approximate 90% of RBPMS+ RGCs and a small number of cones[19], but not other retinal cells, were positive for tdTomato (**Extended Data Fig. 1d, e**).

By generating $CKO^{Dnmt1}$ and $CKO^{Dnmt3a}$, we noted that adult homozygous $CKO^{Dnmt3a-/-}$ mice developed obesity and malocclusion, presumably because *vGlut2* drives *Cre* expression in many CNS neurons. The mice also suffered a high mortality rate from anesthetics during surgical procedures. In contrast, heterozygous $CKO^{Dnmt3a+/-}$ mice grew and bred normally without apparent health concerns or retinal structural changes. This prompted us to focus on *heterozygous CKO* mice. We isolated RGCs using magnetic bead-conjugated Thy-1 antibody and detected significant downregulation of *Dnmt3a* mRNA in heterozygous $CKO^{Dnmt3a+/-}$ RGCs compared to those from the littermate controls (**Extended Data Fig. 1f**). We noted that in homozygous $CKO^{Dnmt3a-/-}$ RGCs, a low level of *Dnmt3a* mRNA was detected, likely because Thy-1 is not exclusively expressed by RGCs in the rodent retinas[20,21]. We confirmed that *Dnmt1* and *Dnmt3a* mRNA levels were downregulated selectively in the RGCs, but not the entire retinas of $CKO^{Dnmt1+/-}$ and $CKO^{Dnmt3a+/-}$ mice, respectively (note that RGCs comprise ~1% of all

retinal cells; **Extended Data Fig. 1f-i**). We studied axonal growth capacity using retinal explant cultures derived from adult *CKO*$^{Dnmt1+/-}$ and *CKO*$^{Dnmt3a+/-}$ mice, and littermate controls that carried *Cre* without *floxed* alleles or *floxed* alleles without *Cre* (**Fig. 1k-n**). While the retinal explants of control mice showed minimal axonal growth, those from adult *CKO*$^{Dnmt3a}$ mice exhibited an over 20-fold increase in axon number (**Fig. 1l**) and at least a 2-fold increase in average axon length (**Fig. 1m**) compared to control mice. The retinal explants of C*KO*$^{Dnmt3a+/-}$ and C*KO*$^{Dnmt3a-/-}$ mice revealed similarly increased number and rate of axon regeneration (data not shown), suggesting that the absence of one *Dnmt3a* allele is sufficient to unleash the barrier to axon regeneration. In contrast, retinal explants of *CKO*$^{Dnmt1+/-}$ mice showed no significant improvement in axonal growth compared to controls (**Fig. 1l and m, Extended Data Fig. 1j**). We further verified that *Dnmt3a* deficiency in *CKO*$^{Dnmt3a+/-}$ RGCs did not have significant impact on the expression of *Dnmt1* (**Extended Data Fig. 1k**) or *Dnmt3b* (**Extended Data Fig. 1l**). In agreement with the downregulation of *Dnmt3a*, reduced DNA methylation was detected in *CKO*$^{Dnmt3a+/-}$ RGCs, but not other retinal cell types compared to controls (**Extended Data Fig. 1m, n**). We concluded that *Dnmt3a*, rather than *Dnmt1*, negatively regulates the intrinsic program for RGC axon growth during maturation.

**Optic nerve reinnervation and restoration of vision by *Dnmt3a* deficiency**

Next, we tested *in vivo* if RGC-specific *Dnmt3a* deficiency restores axons' regenerative capacity in adult RGCs using the optic nerve crush (ONC) injury model. Adult *CKO*$^{Dnmt3a+/-}$ mice, as well as their littermate *Cre* or *floxed* control mice, were subjected to ONC. Axonal regrowth was assessed by labeling RGC axons with cholera toxin B subunit (CTB) two days before mice were sacrificed[9,22]. In control mice, CTB-positive axons were observed only proximal to the crush site (**Fig. 2a**) at all time points examined after ONC, confirming the failure of nerve regeneration. In contrast, numerous RGC axons regenerated across the lesion site for long distances in *CKO*$^{Dnmt3a+/-}$ mice, with many growing more than 3 mm distal to the lesion by 14 days post ONC (**Fig. 2a**). Notably, the number of regenerated axons was so great that in most cases, it was impossible to count the number of regenerating axons in optic nerve sections. We thus quantified axon regeneration by measuring CTB-labeling immunofluorescent intensity at various distances posterior to the crush site. At all distances, we detected at least 3-fold increase in the intensity of CTB-labeling in *CKO*$^{Dnmt3a+/-}$ mice compared to controls; the difference was > 8-fold up to 750 µm distal to the lesion (**Fig. 2b**)**.** Moreover, RGCs of *CKO*$^{Dnmt3a+/-}$ mice displayed a significant increase in survival as evidenced by RBPMS-immunolabeling (50% *vs* 12% at 14 days post-ONC. **Fig. 2c, d**). No signs of RGC proliferation were detected as assessed by EdU

incorporation assays (data not shown), suggesting that the increased RGC number was not due to the birth of new neurons or RGCs.

The regenerating axons continued to grow along the optic nerve over time. As early as 4 weeks following the injury, many regenerating axons grew past the optic chiasm, where a major barrier to RGC axon regeneration and target reinnervation was previously reported[23,24]. Greater fluorescent intensity of labeled axons entered the brain when examined at 8- and 16-weeks post-injury, suggesting continual growth of axons. By 16 weeks post-ONC, a large number of regenerating axons crossed the optic chiasm of the contralateral side (**Fig. 2e, f**). In contrast, no axons were evident in the optic chiasm (**Extended Data Fig. 2a**), optic tract, and brain targets (data not shown) of control mice. Unprecedented numbers of regenerating axons were seen in the optic tract of $CKO^{Dnmt3a+/-}$ mice, primarily extending along the side contralateral to the injury and reinnervating the dorsal and ventral lateral geniculate nuclei (LGN) as well as the pretectum (**Fig. 2g** and **Extended Data Fig. 2b**). These findings show that *Dnmt3a* deficiency in RGCs empowers long-distance and robust optic nerve regeneration and reinnervation into the central visual targets of the optic nerve in adult mice.

We asked if optic nerve reinnervation into the brain targets of adult $CKO^{Dnmt3a+/-}$ mice led to the restoration of RGC function and vision after ONC (**Fig. 3a**). We assessed mouse visual function by measuring the optomotor response (OMR), which uses the head tracking behavior of mice to determine their spatial vision (e.g., visual acuity)[25]. Normal mice without the injury typically exhibited a visual acuity of 0.4 – 0.5 cycle/degree as measured by OMR. When examined at 2 weeks post ONC, all animals exhibited a complete loss of head tracking behavior in OMR assays, indicative of blindness following nerve injury (**Fig. 3b**). OMR remained absent in control mice throughout the study period (up to 16 weeks post-lesion). In contrast, ~40% of the $CKO^{Dnmt3a+/-}$ mice started to show a recovery of OMR by 4 weeks post-injury, a time corresponding to the entry of RGC axons into the brain and reinnervating the central visual targets as documented above. The percentage of $CKO^{Dnmt3a+/-}$ mice which had regained OMR increased with time and reached ~70% by 16 weeks post-ONC. Quantification of OMR-based visual acuity reached 0.26 cycle/degree, a recovery of more than 50% of the normal value of visual acuity in mice (**Fig. 3b**).

We performed additional assays to evaluate the RGC and visual functions. First, in a dark/light preference assay, normal mice spent over 80% of their time in a dark environment. Whereas

wildtype mice subjected to ONC showed no preference for a dark environment when examined up to 16 weeks post-injury. In contrast, this response in *CKO*$^{Dnmt3a+/-}$ mice with ONC recovered to the same level as observed in uninjured mice by 16 weeks post injury (**Fig. 3c**), clear indication of a restoration of light perception. Second, we measured visually evoked potentials (VEPs) in the cortex. Control mice showed an absence of or flat VEP N1 wave (with an infinite delay of N1 latency; **Fig. 3d** and **Extended Data Fig. 2c, d**) up to 16 weeks after nerve crush. Whereas, in parallel with the OMR recovery, ~60% of *CKO*$^{Dnmt3a+/-}$ mice regained VEP N1 responses at an amplitude to half of its baseline value by 16 weeks post-injury (**Fig. 3d; Extended Data Fig. 2d**). Of note, there was a significant delay in N1 latency in *CKO*$^{Dnmt3a+/-}$ mice after injury compared to the normal uninjured group (**Extended Data Fig. 2c, d**), potentially due to immature synaptic reconnection or incomplete myelination of the regenerated axons that should impede the speed of electrical signal transmission from the eye to the brain[26,27]. Moreover, significant increases in the amplitude of positive scotopic threshold response (pSTR)[28], a readout of the electrical activity of RGCs, was detected in *CKO*$^{Dnmt3a+/-}$ mice during the period of 4 – 16 weeks post-injury when compared to control mice (**Fig. 3e; Extended Data Fig. 2e**). Together, these results demonstrated reversal of RGC function and vision loss following axon regeneration in a crush-injured optic nerve in adult mice via a single gene manipulation.

**Wide-scale transcriptome shifts by various RGC types towards an injury resilient and regenerative status**

Because mouse retina contains 45 RGC types that differ dramatically in their survival and regenerative ability following ONC[18], it is important to understand if *Dnmt3a* deficiency promotes axon regeneration of specific RGC types. To address the question, we asked if *Dnmt3a* deficiency shifts the RGC landscape or alters the injury responses (pathophysiological condition) in selective RGC types by profiling the RGC transcriptome using single nuclei RNA sequencing (snRNA-seq). Retinas were collected at 2 days post-injury, when few if any RGCs have died but responses to injury are already apparent[5,29]. RGC nuclei were enriched by fluorescence-activated cell sorting (FACS) with a NeuN antibody and profiled by droplet-based snRNA-seq using the 10X platform[30]. We first examined if the proportions of RGC types was affected by *Dnmt3a* deficiency. In the retinas of both *CKO*$^{Dnmt3a+/-}$ and control mice, we observed 35 RGC clusters, within which 42 of the 45 reported RGC types were identified based on the RGC atlas markers[18,29] (**Fig. 3f-h** and **Extended data Fig. 3a-c**). More than half of the clusters (24/35) were 1:1 matches with the reported atlas RGC types, while the other 11 each contained 2-4

RGC types (**Fig. 3h**). The mixture of RGC types within clusters is likely due to the smaller number of RGCs profiled here compared to the earlier report. We found virtually no differences in the distribution of RGC clusters between *CKO*$^{Dnmt3a+/-}$ and control mice (**Fig. 3g**). Over 90% of RGC clusters showed similar frequencies in *CKO*$^{Dnmt3a+/-}$ and control mice (**Fig. 3f-h** and **Extended Data Fig. 3a-c**). Notably, the frequencies of three αRGC subsets (αON-S/M4|αON-T, αOFF-S and αOFF-T|αON-T), which are the rarest and the most vulnerable and regenerative RGC types[31,32], were slightly increased in *CKO*$^{Dnmt3a+/-}$ mice compared to controls. They collectively represented ~6% of the total RGC population in *CKO*$^{Dnmt3a+/-}$ mice compared to <3% in control mice (**Extended Data Fig. 3c**). Collectively, DNMT3a deficiency does not alter the distribution of retinal cell and RGC profiles or drastically changes the frequencies of the vast majority of RGC types except it somewhat increases the occurrence of rare αRGC subsets.

With this assurance, we assessed differences in gene expression changes after ONC between control and *CKO*$^{Dnmt3a+/-}$ RGCs. In line with the robust optic nerve regeneration, we observed upregulation of the nerve growth-related pathways as classified by Gene Ontology (GO) terms, including optic nerve morphogenesis, axonogenesis and dendrite extension (**Fig. 3i**). In contrast, genes associated with neuron death, axon injury response, and neuroinflammation signals classified by GO terms, were downregulated compared to controls, indicating enhanced resilience to injury. By combining the normalized enrichment scores (NES) of injury response- and growth-regulated gene categories, respectively, in each individual RGC clusters, we noted a consistent pattern of gene expression changes across a broad spectrum of RGC types (**Fig. 3j** and **Extended Data Fig. 3d, 4a, b, 5a, HTML File**), indicating cell type-independent transformation into growth-promoting and injury-resilient states. Surprisingly, comprehensive downregulation of *Pten* expression, a well-established endogenous inhibitor of axon regeneration which deletion promotes selective axon regeneration of αRGCs[33,34], was not observed in the majority of *CKO*$^{Dnmt3a+/-}$ RGC types, except in four clusters (**Extended Data Fig. 5b**). Moreover, only two *CKO*$^{Dnmt3a+/-}$ RGC clusters displayed significantly decreased expression of *Socs3*, another well-known axon regeneration inhibitor[29,34], when compared to controls. These findings suggest that *CKO*$^{Dnmt3a+/-}$ mice switch on a *Pten*- or *SOCS3*-independent axon growth mechanism. Contrary to promoting nerve regeneration in selective RGC types, *Dnmt3a* deficiency triggers a broad-spectrum RGC-transcriptome shift toward a gene profile associated with axon regeneration in nearly all RGC types, including those previously shown to be susceptible to injury (e.g., C35, C25/C34) and those relatively resilient to injury (e.g., αRGCs, M1-RGCs)[18]. Thus, *Dnmt3a* deficiency results in a wide-scale change of transcriptome profiles

in various RGC types toward injury-resilient, less inflammatory, and pro-regenerative states after ONC.

**Multifaceted induction of axon regeneration machinery in *Dnmt3a* deficient RGCs**

The inability of RGC axons to regenerate is believed to stem from a complex interplay of intrinsic factors and environmental cues, with CNS glial cells releasing axon growth-inhibitory signals and posing a formidable barrier to axon regeneration[1]. To gain deeper insights into the signaling mechanisms through which RGC-specific *Dnmt3a* deficiency disinhibits the development of glial barrier to axonal regrowth, we employed CellChat analysis, a bioinformatic algorithm designed to predict and decipher intercellular cues exchanged by various cell types[35]. Given that DNMT3a dysfunction in $CKO^{Dnmt3a+/-}$ mice is RGC-specific, we focused on outgoing signals from RGCs to other cell types identified in our snRNA-seq (**Fig. 3f**). As shown above, CellChat analysis consistently predicted significant downregulation of RGC-derived inflammatory signals in $CKO^{Dnmt3a+/-}$ mice compared to controls, primarily associated with three immune activator (**Fig. 4a** and **Extended Data Fig. 6a, b**): colony stimulating factor (CSF)[28], granulin (GRN)[36], and major histocompatibility complex class 1 (MHC-1)[37]. Notably, the chord diagram showed that in control mice, CSF originating from the RGCs signaled to multiple other retinal cell classes, especially immune cells, whereas this RGC signal was drastically diminished in the $CKO^{Dnmt3a+/-}$ mice (**Fig. 4b**). *Dnmt3a* deficiency also led to downregulation of axon growth-inhibitory signals, such as Semaphorin 4 (SEMA4)[38], and upregulation of synapse and axon growth-promoting signals, angiopoietin (ANGPT)[39,40] and secreted phosphoprotein 1/osteopontin (SPP1)[41] (**Fig. 4a**). Therefore, RGC-specific *Dnmt3a* deficiency not only induces an intrinsic pro-regenerative program within RGCs but also enables a permissive environment by sending decreased inflammatory signals and increased growth-promoting signals.

To determine how *Dnmt3a* deficiency alters the communication among RGC types, we also compared CellChat signaling among RGCs in $CKO^{Dnmt3a+/-}$ and control mice. The results indicated the up-regulation of classical *Wnt*[42] and non-canonical *Wnt*[43], PDGF and FGF signaling[44] by many RGC types in $CKO^{Dnmt3a+/-}$ mice compared to controls (**Fig. 4c** and **Extended Data Fig. 7a, b**). The chord diagram of the WNT communication indicated that intrinsically photosensitive RGC types M1a and M2 are the sole major source of WNT signal in controls, while in $CKO^{Dnmt3a+/-}$ mice, multiple RGC types upregulate outgoing WNT signaling to other RGCs (**Fig. 4d**). $CKO^{Dnmt3a+/-}$ RGCs also exhibited distinctive expression of poliovirus receptor (PVR)[45,46] and visfatin[47,48], two growth and survival-related genes that were absent in

control RGCs. Conversely, the growth factors with pro-inflammatory properties, such as vascular endothelial growth factor (VEGF)[49] and interleukin 4[50,51], were highly expressed only in control RGCs but not in *CKO*$^{Dnmt3a+/-}$ RGCs (**Fig. 4c**). These results strengthen the conclusion that *Dnmt3a* deficiency in the RGC contributes to distinctive pro-regenerative intercellular signaling and suppressed inflammatory responses.

**DNA methylation of axon growth gene networks regulated by *Dnmt3a***

DNMT mediates DNA methylation to serve biological functions. To investigate how *Dnmt3a* deficiency altered the landscape of DNA methylation in RGCs, we conducted whole genome bisulfite sequencing (WGBS) of RGCs isolated 2 days post-ONC. Compared to controls, *CKO*$^{Dnmt3a+/-}$ RGCs showed lower CG methylation levels specifically in the differentially methylated regions (DMRs) (**Fig. 4e**), which are the genomic regions show different methylation status between individuals. DMRs are highly regarded as possible functional regions involved in gene transcriptional regulation[52]. In contrast, minimal alteration in genome-wide DNA methylation level was detected comparing the two groups (**Extended Data Fig. 8a, b**). WGBS disclosed 4,836 CG DMRs, including 4,004 hypo-DMRs and 832 hyper-DMRs (**Extended data Fig. 8c**). Annotation of the hypomethylated DMR-related genes identified 48 pathways in the biological processes, which reflect the aforementioned transcriptomic shifts toward a pro-regenerative state in the *CKO*$^{Dnmt3a+/-}$ RGCs. Fourteen of these hypomethylated pathways are linked to axon growth, including axon guidance, axonogenesis and axon development (e.g., *Wnt3, Klf7, Map2*)[38,53,54], and 6 are related to synaptic process (e.g., *UNC13a* and *Nrxn1*)[55,56] (**Fig. 4f**). KEGG pathway analysis of total DMR-related genes again depicted distinctive enrichment in pathways related to nerve growth and synaptic process that include key signaling events such as *Wnt*, *Ras*, and *cAMP*, axon guidance, and dopaminergic and glutamatergic synapse (**Fig. 4g**). The data establish that DNMT3a directly regulates the methylation of gene networks that control axon growth and synaptic process.

To validate that hypomethylation of genes controlling axon growth and synaptic process in *Dnmt3a*-deficient mice results in correspondent gene expression changes, we conducted comprehensive transcriptome profiling by bulk RNA-seq on RGCs isolated two days after ONC. Principal component analysis clearly separated *CKO*$^{Dnmt3a+/-}$ RGCs from the controls (**Extended Data Fig. 8d**). We identified 1,459 genes that are differentially expressed (DEGs) (Fold change > 1.5; padj < 0.05) between *CKO*$^{Dnmt3a+/-}$ and control RGCs (**Extended Data Fig. 8e**). KEGG analyses revealed alignment between upregulated gene pathways in *CKO*$^{Dnmt3a+/-}$ RGCs with

those found to be hypomethylated above, including synaptic signaling and axon guidance (**Fig. 4h**). On the other hand, downregulated DEGs in the *CKO*$^{Dnmt3a+/-}$ RGCs were primarily involved in cell death and immune regulation, such as apoptosis, TNFα and chemokine/cytokine signaling (**Extended Data Fig. 9a**). GSEA and GO enrichment studies confirmed the results of KEGG analysis, showing downregulation of immune response (e.g., T cell and macrophage migration, chemokine-mediated signaling, and microglial activation) and inflammatory gene pathways (e.g., IFNγ, TNFα, and IL6-JAK-STAT3 signaling)[57] with concurrent upregulation of key events regulating axon growth (e.g., *Wnt/β-catenin*) and synaptic assembling and transport (**Extended Data Fig. 9b, c**). This result was congruent with the prediction of CellChat analysis.

We further verified the gene expression pattern changes detected by bulk RNA-seq in *CKO*$^{Dnmt3a+/-}$ and control mice by qPCR. *CKO*$^{Dnmt3a+/-}$ RGCs isolated at 2 days post-injury showed consistent significant differences in the expression of the aforementioned gene pathways, including the upregulation of axon growth-related genes (e.g., *mTOR*, *Spp1*, *Gap43*) and downregulation of growth inhibitors (e.g. *Atf3*) as well as cell apoptotic and inflammatory genes (e.g., *Gas5*, *Casp3*, *Casp8*, *Ripk1*)[1,29,57,58] compared to control RGCs (**Fig. 4i**). Interestingly, these differences were only detected in RGCs isolated post ONC. RGCs taken from uninjured *CKO*$^{Dnmt3a+/-}$ mice showed no significant differences in expression of any of these genes compared to RGCs from uninjured control mice (**Fig. 4i**). The data suggest that the loss of DNMT3a driven by *Vglut2-Cre* has little impact on gene expression of normal RGCs but rather results in reprogramming of RGCs' injury responses toward an injury-resilient and pro-regenerative status post-ONC. Together, these studies demonstrated that *Dnmt3a* deficiency reshaped the injury-induced transcriptomic and intercellular communication landscape of RGCs, contributing to the functional regeneration of the optic nerve.

**Therapeutic inhibition of *Dnmt3a* rescued visual function in adult wildtype mice after ONC**

To assess the therapeutic potential of *Dnmt3a* inhibition, we conducted AAV treatment experiments in adult mice after ONC (**Fig. 5a**). To downregulate *Dnmt3a* we injected AAV-shRNA intravitreally to adult wildtype mice or AAV-Cre to mice carrying heterozygous floxed *Dnmt3a* allele (*fl/+*) immediately after ONC. Detection of GFP expression revealed wide-spread AAV-infection in RGCs, and qPCR analysis confirmed the downregulation of *Dnmt3a* mRNA levels in RGCs of eyes injected with AAV-shRNA or AAV-Cre compared to AAV-scrambled RNA or AAV-GFP injected eyes (**Extended data fig. 9d, e**). Tracking of the spatial vision with OMR

at multiple timepoints post-injury indicated partial recovery of visual acuity in over 50% of mice received AAV-shRNA treatment starting at 6 weeks post-injury (**Fig. 5a, b**), a two-week delay of recovery than that was seen in *CKO*$^{Dnmt3a+/-}$ mice above. This corresponds to the two week-time period that is required for AAV to reach its peak/plateau of gene expression after intravitreal injection (not shown). In contrast, control mice received injection of AAV-scrambled RNA showed no response in the OMR test up to 12 weeks after injury. By 12 weeks post-ONC, AAV-shRNA-treated mice regained light perception and exhibited no difference in light/dark box assays compared to their uninjured baselines (**Fig. 5c**). Moreover, AAV-shRNA-treated mice demonstrated improved pSTR and N1 amplitude of VEP compared to control mice receiving AAV-scrambled RNA injection, which remained blind without any sign of light perception or VEP response (**Fig. 5d-f**)**.** Similar recovery of visual acuity, light perception, pSTR, and VEP improvement were also observed in *fl/+* mice received AAV-Cre compared to AAV-GFP injected mice (**Fig. 5g-m**)**.** Similarly, delays in VEP N1 latency were observed in both AAV-shRNA-treated wildtype mice and *AAV-Cre*-injected *fl/+* mice, suggesting impaired myelination. These results provide compelling evidence that *Dnmt3a* inhibition holds immense therapeutic potential for the treatment of optic nerve diseases or injury, offering a viable avenue for restoring vision *in vivo*.

## Discussion

Here we report restoration of vision after traumatic injury of the optic nerve via suppression of *Dnmt3a*, which can overcome the inability of adult RGCs to regenerate axons. Inhibition of DNMT3a-dependent DNA methylation reactivates an intrinsic axon growth program that is lost in adults, promotes RGC survival, and enables axonal regeneration through the optic nerve to central targets. As regenerating axons reach the brain, spatial vision is recovered. This finding highlights the dominant role played by neuron-intrinsic determinants in driving functional optic nerve regeneration and alleviating environmental obstacles, likely through signaling from RGCs to other cell classes and to each other. Moreover, *Dnmt3a* deficiency facilitates selective demethylation of gene networks and multifaced activation of axon growth machinery across diverse RGC subtypes without apparent neuroinflammation or compromised neuronal survival. Most importantly, therapeutic suppression of *Dnmt3a*, either by AAV-shRNA delivery or other means, holds the potential for clinical translation. This discovery not only offers an exciting avenue for treating injury to optic nerve diseases and injury, but also paves the way for future research in brain and spinal cord regeneration.

**Acknowledgements**

This work was supported by the National Eye Institute Grant R01 EY031696, R21 EY033882 and a Harvard NeuroDiscovery Center Grant to D.F.C., a Core Grant for Vision Research from NIH/NEI to the Schepens Eye Research Institute (P30EY003790), and R21 EY032219 to J.R.S. We thank Haobo Li for plasmid construction and AAV production; Jenna Cho, Alice An, and Irvine Yi for assistance in data quantification; Anton Lennikov, Shuhong Jiang, and Karen Chang for advice and assistance in imaging and visual function studies; Kasim Gunes and Julie Chen for support in culture studies. We thank the Schepens Eye Institute Animal Care Facilities for support in the animal studies, the Gene Transfer Vector Core, and the Morphology Core facility, which is supported by the NIH-National Eye Institute P30 Core Grant (P30EY003790).

**Author contributions**

D.F.C and W.L.T. perceived the project, analyzed the data, and wrote and revised the manuscript with input from all co-authors. W.L.T. was involved in all experiments and analyses. K.C. contributed to the optic nerve crush studies and trained W.L.T. in all animals works and analyses. E.K. designed and performed all sequencing data computational analysis. A.M. performed single-nucleus RNA sequencing and W.Y. contributed to single-nucleus data preprocessing. A.A. contributed to the culture studies and assisted with image acquisition. Y.L. and X.W. conducted early small-molecule and genetic screening studies. T.P.G. contributed to qPCR and morphometric analyses. J.R.S and P.B. carefully read and edited the manuscript and supervised single-nucleus RNA sequencing studies.

**Competing interests**

The other authors declare no competing interests.

1 Varadarajan, S. G., Hunyara, J. L., Hamilton, N. R., Kolodkin, A. L. & Huberman, A. D. Central nervous system regeneration. *Cell* **185**, 77-94 (2022). https://doi.org:10.1016/j.cell.2021.10.029

2 Williams, P. R., Benowitz, L. I., Goldberg, J. L. & He, Z. Axon Regeneration in the Mammalian Optic Nerve. *Annu Rev Vis Sci* **6**, 195-213 (2020). https://doi.org:10.1146/annurev-vision-022720-094953

3 Kristensen, L. S., Nielsen, H. M. & Hansen, L. L. Epigenetics and cancer treatment. *Eur J Pharmacol* **625**, 131-142 (2009). https://doi.org:10.1016/j.ejphar.2009.10.011

4 Chen, D. F. & Tonegawa, S. Why do mature CNS neurons of mammals fail to re-establish connections following injury--functions of bcl-2. *Cell Death Differ* **5**, 816-822 (1998). https://doi.org:10.1038/sj.cdd.4400431

5 Chen, D. F., Schneider, G. E., Martinou, J. C. & Tonegawa, S. Bcl-2 promotes regeneration of severed axons in mammalian CNS. *Nature* **385**, 434-439 (1997).

6 Chen, D. F., Jhaveri, S. & Schneider, G. E. Intrinsic changes in developing retinal neurons result in regenerative failure of their axons. *Proc Natl Acad Sci U S A* **92**, 7287-7291 (1995). https://doi.org:10.1073/pnas.92.16.7287

7 Goldberg, J. L., Klassen, M. P., Hua, Y. & Barres, B. A. Amacrine-signaled loss of intrinsic axon growth ability by retinal ganglion cells. *Science* **296**, 1860-1864 (2002). https://doi.org:10.1126/science.1068428

8 Rao, R. C. *et al.* Dynamic patterns of histone lysine methylation in the developing retina. *Invest Ophthalmol Vis Sci* **51**, 6784-6792 (2010). https://doi.org:10.1167/iovs.09-4730

9 Lu, Y. *et al.* Reprogramming to recover youthful epigenetic information and restore vision. *Nature* **588**, 124-129 (2020). https://doi.org:10.1038/s41586-020-2975-4

10 Juarez-Mercado, K. E. *et al.* Expanding the Structural Diversity of DNA Methyltransferase Inhibitors. *Pharmaceuticals (Basel)* **14** (2020). https://doi.org:10.3390/ph14010017

11 Day, J. J. & Sweatt, J. D. DNA methylation and memory formation. *Nat Neurosci* **13**, 1319-1323 (2010). https://doi.org:10.1038/nn.2666

12 Ji, Y., Zhao, M., Qiao, X. & Peng, G. H. Decitabine improves MMS-induced retinal photoreceptor cell damage by targeting DNMT3A and DNMT3B. *Front Mol Neurosci* **15**, 1057365 (2022). https://doi.org:10.3389/fnmol.2022.1057365

13 Farinelli, P. *et al.* DNA methylation and differential gene regulation in photoreceptor cell death. *Cell Death Dis* **5**, e1558 (2014). https://doi.org:10.1038/cddis.2014.512

14 Chen, Z. & Zhang, Y. Role of Mammalian DNA Methyltransferases in Development. *Annu Rev Biochem* **89**, 135-158 (2020). https://doi.org:10.1146/annurev-biochem-103019-102815

15 Jackson-Grusby, L. *et al.* Loss of genomic methylation causes p53-dependent apoptosis and epigenetic deregulation. *Nat Genet* **27**, 31-39 (2001). https://doi.org:10.1038/83730

16 Kaneda, M. *et al.* Essential role for de novo DNA methyltransferase Dnmt3a in paternal and maternal imprinting. *Nature* **429**, 900-903 (2004). https://doi.org:10.1038/nature02633

17 Vong, L. *et al.* Leptin action on GABAergic neurons prevents obesity and reduces inhibitory tone to POMC neurons. *Neuron* **71**, 142-154 (2011). https://doi.org:10.1016/j.neuron.2011.05.028

18 Tran, N. M. *et al.* Single-Cell Profiles of Retinal Ganglion Cells Differing in Resilience to Injury Reveal Neuroprotective Genes. *Neuron* **104**, 1039-1055 e1012 (2019). https://doi.org:10.1016/j.neuron.2019.11.006

19 Wassle, H., Regus-Leidig, H. & Haverkamp, S. Expression of the vesicular glutamate transporter vGluT2 in a subset of cones of the mouse retina. *J Comp Neurol* **496**, 544-555 (2006). https://doi.org:10.1002/cne.20942

20 Barnstable, C. J. & Drager, U. C. Thy-1 antigen: a ganglion cell specific marker in rodent retina. *Neuroscience* **11**, 847-855 (1984). https://doi.org:10.1016/0306-4522(84)90195-7

21 Perry, V. H., Morris, R. J. & Raisman, G. Is Thy-1 expressed only by ganglion cells and their axons in the retina and optic nerve? *J Neurocytol* **13**, 809-824 (1984). https://doi.org:10.1007/BF01148495

22 Cho, K. S. *et al.* Re-establishing the regenerative potential of central nervous system axons in postnatal mice. *J Cell Sci* **118**, 863-872 (2005). https://doi.org:10.1242/jcs.01658

23 Pernet, V. & Schwab, M. E. Lost in the jungle: new hurdles for optic nerve axon regeneration. *Trends Neurosci* **37**, 381-387 (2014). https://doi.org:10.1016/j.tins.2014.05.002

24 Conceicao, R. *et al.* Expression of Developmentally Important Axon Guidance Cues in the Adult Optic Chiasm. *Invest Ophthalmol Vis Sci* **60**, 4727-4739 (2019). https://doi.org:10.1167/iovs.19-26732

25 Shi, C. *et al.* Optimization of Optomotor Response-based Visual Function Assessment in Mice. *Sci Rep* **8**, 9708 (2018). https://doi.org:10.1038/s41598-018-27329-w

26 Ridder, W. H., 3rd & Nusinowitz, S. The visual evoked potential in the mouse--origins and response characteristics. *Vision Res* **46**, 902-913 (2006). https://doi.org:10.1016/j.visres.2005.09.006

27 You, Y., Klistorner, A., Thie, J. & Graham, S. L. Latency delay of visual evoked potential is a real measurement of demyelination in a rat model of optic neuritis. *Invest Ophthalmol Vis Sci* **52**, 6911-6918 (2011). https://doi.org:10.1167/iovs.11-7434

28 Tang, Y. *et al.* Therapeutic Targeting of Retinal Immune Microenvironment With CSF-1 Receptor Antibody Promotes Visual Function Recovery After Ischemic Optic Neuropathy. *Front Immunol* **11**, 585918 (2020). https://doi.org:10.3389/fimmu.2020.585918

29 Jacobi, A. *et al.* Overlapping transcriptional programs promote survival and axonal regeneration of injured retinal ganglion cells. *Neuron* **110**, 2625-2645 e2627 (2022). https://doi.org:10.1016/j.neuron.2022.06.002

30 Hahn, J. *et al.* Evolution of neuronal cell classes and types in the vertebrate retina. *bioRxiv* (2023). https://doi.org:10.1101/2023.04.07.536039

31 Lim, J. H. *et al.* Neural activity promotes long-distance, target-specific regeneration of adult retinal axons. *Nat Neurosci* **19**, 1073-1084 (2016). https://doi.org:10.1038/nn.4340

32 Duan, X. *et al.* Subtype-specific regeneration of retinal ganglion cells following axotomy: effects of osteopontin and mTOR signaling. *Neuron* **85**, 1244-1256 (2015). https://doi.org:10.1016/j.neuron.2015.02.017

33 Rheaume, B. A. *et al.* Pten inhibition dedifferentiates long-distance axon-regenerating intrinsically photosensitive retinal ganglion cells and upregulates mitochondria-associated Dynlt1a and Lars2. *Development* **150** (2023). https://doi.org:10.1242/dev.201644

34 Sun, F. *et al.* Sustained axon regeneration induced by co-deletion of PTEN and SOCS3. *Nature* **480**, 372-375 (2011). https://doi.org:10.1038/nature10594

35 Jin, S. *et al.* Inference and analysis of cell-cell communication using CellChat. *Nat Commun* **12**, 1088 (2021). https://doi.org:10.1038/s41467-021-21246-9

36 Park, B. *et al.* Granulin is a soluble cofactor for toll-like receptor 9 signaling. *Immunity* **34**, 505-513 (2011). https://doi.org:10.1016/j.immuni.2011.01.018

37 Rao, K. & Lund, R. D. Optic nerve degeneration induces the expression of MHC antigens in the rat visual system. *J Comp Neurol* **336**, 613-627 (1993). https://doi.org:10.1002/cne.903360413

38 Carulli, D., de Winter, F. & Verhaagen, J. Semaphorins in Adult Nervous System Plasticity and Disease. *Front Synaptic Neurosci* **13**, 672891 (2021). https://doi.org:10.3389/fnsyn.2021.672891

39 Zhou, H. *et al.* Angiopoietin-2 induces the neuronal differentiation of mouse embryonic NSCs via phosphatidylinositol 3 kinase-Akt pathway-mediated phosphorylation of mTOR. *Am J Transl Res* **11**, 1895-1907 (2019).

40 Luck, R. *et al.* The angiopoietin-Tie2 pathway regulates Purkinje cell dendritic morphogenesis in a cell-autonomous manner. *Cell Rep* **36**, 109522 (2021). https://doi.org:10.1016/j.celrep.2021.109522

41 Li, S. & Jakobs, T. C. Secreted phosphoprotein 1 slows neurodegeneration and rescues visual function in mouse models of aging and glaucoma. *Cell Rep* **41**, 111880 (2022). https://doi.org:10.1016/j.celrep.2022.111880

42 Garcia, A. L., Udeh, A., Kalahasty, K. & Hackam, A. S. A growing field: The regulation of axonal regeneration by Wnt signaling. *Neural Regen Res* **13**, 43-52 (2018). https://doi.org:10.4103/1673-5374.224359

43 Musada, G. R., Carmy-Bennun, T. & Hackam, A. S. Identification of a Novel Axon Regeneration Role for Noncanonical Wnt Signaling in the Adult Retina after Injury. *eNeuro* **9** (2022). https://doi.org:10.1523/ENEURO.0182-22.2022

44 Johnson, T. V. *et al.* Identification of retinal ganglion cell neuroprotection conferred by platelet-derived growth factor through analysis of the mesenchymal stem cell secretome. *Brain* **137**, 503-519 (2014). https://doi.org:10.1093/brain/awt292

45 Ikeda, W. *et al.* Nectin-like molecule-5/Tage4 enhances cell migration in an integrin-dependent, Nectin-3-independent manner. *J Biol Chem* **279**, 18015-18025 (2004). https://doi.org:10.1074/jbc.M312969200

46 Kajita, M., Ikeda, W., Tamaru, Y. & Takai, Y. Regulation of platelet-derived growth factor-induced Ras signaling by poliovirus receptor Necl-5 and negative growth regulator Sprouty2. *Genes Cells* **12**, 345-357 (2007). https://doi.org:10.1111/j.1365-2443.2007.01062.x

47 Erfani, S. *et al.* Nampt/PBEF/visfatin exerts neuroprotective effects against ischemia/reperfusion injury via modulation of Bax/Bcl-2 ratio and prevention of caspase-3 activation. *J Mol Neurosci* **56**, 237-243 (2015). https://doi.org:10.1007/s12031-014-0486-1

48 Erfani, S. *et al.* Visfatin reduces hippocampal CA1 cells death and improves learning and memory deficits after transient global ischemia/reperfusion. *Neuropeptides* **49**, 63-68 (2015). https://doi.org:10.1016/j.npep.2014.12.004

49 Carmeliet, P. Mechanisms of angiogenesis and arteriogenesis. *Nat Med* **6**, 389-395 (2000). https://doi.org:10.1038/74651

50 Daines, J. M., Schellhardt, L. & Wood, M. D. The Role of the IL-4 Signaling Pathway in Traumatic Nerve Injuries. *Neurorehabil Neural Repair* **35**, 431-443 (2021). https://doi.org:10.1177/15459683211001026

51 Milner, J. D. *et al.* Sustained IL-4 exposure leads to a novel pathway for hemophagocytosis, inflammation, and tissue macrophage accumulation. *Blood* **116**, 2476-2483 (2010). https://doi.org:10.1182/blood-2009-11-255174

52 Rakyan, V. K., Down, T. A., Balding, D. J. & Beck, S. Epigenome-wide association studies for common human diseases. *Nat Rev Genet* **12**, 529-541 (2011). https://doi.org:10.1038/nrg3000

53 Patel, A. K., Park, K. K. & Hackam, A. S. Wnt signaling promotes axonal regeneration following optic nerve injury in the mouse. *Neuroscience* **343**, 372-383 (2017). https://doi.org:10.1016/j.neuroscience.2016.12.020

54 Plachez, C. *et al.* Robos are required for the correct targeting of retinal ganglion cell axons in the visual pathway of the brain. *Mol Cell Neurosci* **37**, 719-730 (2008). https://doi.org:10.1016/j.mcn.2007.12.017

55 Sudhof, T. C. Neuroligins and neurexins link synaptic function to cognitive disease. *Nature* **455**, 903-911 (2008). https://doi.org:10.1038/nature07456

56 Yang, Y. & Calakos, N. Munc13-1 is required for presynaptic long-term potentiation. *J Neurosci* **31**, 12053-12057 (2011). https://doi.org:10.1523/JNEUROSCI.2276-11.2011

57 Levkovitch-Verbin, H. Retinal ganglion cell apoptotic pathway in glaucoma: Initiating and downstream mechanisms. *Prog Brain Res* **220**, 37-57 (2015). https://doi.org:10.1016/bs.pbr.2015.05.005

58 Han, X. *et al.* Gas5 inhibition promotes the axon regeneration in the adult mammalian nervous system. *Exp Neurol* **356**, 114157 (2022). https://doi.org:10.1016/j.expneurol.2022.114157

## Methods

### Mice

*Vglut2-ires-Cre* knock-in (*Vglut2-Cre*) mice were generated in Bradford B Lowell's laboratory (Harvard University)[1] and *Dnmt3a* floxed (*Dnmt3a*$^{flox}$) mice were obtained from Guoping Fan's laboratory (University of California, Los Angeles)[2]. C57BL/6J wildtype (000664) and B6.Cg-Gt(ROSA)26Sortm9(CAG-tdTomato)Hze/J (007909) mice were purchased from the Jackson Laboratory. Both sexes of animals were used in the experiments. The control group for experiments with Cre/lox mice included *Vglut2-Cre*, floxed, and littermate wildtype mice. All animal procedures are approved by the Institutional Animal Care and Use Committees (IACUCs) at the Schepens Eye Research Institute (SERI), Mass Eye and Ear. Animals were bred and housed under 12-h light/dark cycles with food and water ad libitum in the SERI animal facility.

### RGC isolation

As described previously[3], mouse retinas were dissected in Neurobasal-A medium (Gibco, 10888-022) on ice and dissociated into single-cell suspensions in papain supplemented with deoxyribonuclease I and Ovomucoid protease inhibitor by manual trituration according to the manufacturer's protocol (Papain Dissociation System, Worthington, Lk003150). The resulting cells were spun down and resuspended in autoMACS Rinsing Solution (Miltenyi Biotec, 130-091-222) followed by incubation with micro-magnetic beads conjugated Thy1.2 antibody (Miltenyi Biotec, 130-121-278) for 20 min at 4°C. Cells were then loaded into the MS Column (Miltenyi Biotec, 130-042-201) held by a magnetic separator (Miltenyi Biotec, 130-042-108) that allowed separation of magnetic beads-labeled cells from the rest by rinsing the column. After 3 washings, the column was removed from the separator and the labeled cells were gently flushed into a collection tube with 1 ml of the rinsing solution. The collected cells were spun down and processed for RNA or DNA analysis.

### Total nucleic acids extraction

Total RNA and DNA were extracted using the Zymo Quick-RNA MicroPrep Kit (Zymo Research, R1051) and Quick-DNA MiniPrep Kit (Zymo Research, D3024) respectively. The quantity and quality of both nucleic acids were measured using a NanoDrop 2000 Spectrophotometer (Thermo Fisher Scientific). RNA was then frozen and sent to Novogene for ultra-low-input bulk RNA sequencing or converted into cDNA with the PrimeScript RT Master Mix (Takara Bio, RR036A) for quantification of mRNA level using qPCR[4]. Primers used for qPCR are listed **in**

**Supplementary Table 1**. DNA was frozen and sent to Novogene for whole genome bisulfite sequencing (WGBS) or processed for assessment of global methylation level.

**Global DNA methylation assay**

Genome-wide DNA methylation levels were determined using the 5-mC DNA ELISA Kit (Zymo Research, D5325) per the manufacturer's instruction. Absorbance was recorded at 405 nm with a microplate reader (Agilent, BioTek Synergy H1 Multimode Reader). The percentage of methylated cytosines (% 5-mC) in the total DNA content was determined by calculating the levels of 5-mC using a standard curve generated with the kit controls.

**Human eye globes**

The Lions Eye Bank in Florida provided human cadaver eye globes for the experiments. These eye globes were obtained from donors between the ages of 68 and 92, as stated in **Supplementary Table 2**. All experiments involving human tissue were conducted according to the principles of the Declaration of Helsinki.

**Retinal explant culture**

Retinas dissected out from post-mortem human eyes were cut at both central and peripheral areas with a biopsy punch (Acuderm Inc, P2525) in ice-cold Neurobasal-A medium, producing small explants in 2.5 mm diameter. Retinas from adult mice were cut into 4-6 equally sized pieces. With the RGC layer facing down, retinal explants were placed onto tissue culture inserts (6-well plate format, Greiner Bio-One, 657641) that were pre-coated with Matrigel matrix (Corning, 354230). Inserts were then placed into culture plate wells containing Neurobasal-A medium supplemented with 25 µM L-Glutamic acid (Sigma-Aldrich, G8415), 2 mM Glutamax (Gibco, 35050061), 1× penicillin/streptomycin (Thermo Scientific, 15140122), 1× B-27a (Gibco, 17504-044), 5 µg/ml insulin (Sigma-Aldrich, I9278), 50 ng/ml BDNF (PeproTech, 450-02), 50 ng/ml CNTF (PeproTech, 450-13), and 1× forskolin (Sigma-Aldrich, F6886). Explants were cultured at 37°C with 5% $CO_2$ for 7 days and then processed for immunohistochemical analysis.

**Quantification of neurite outgrowth in explant cultures**

After 7 days of incubation, retinal explants on inserts were fixed with 4% PFA for 2 h and blocked with Mojito buffer (10% NGS, 3% NDS, 1% BSA, 0.5% Tween-20, 0.5% Triton X-100 and 0.1% sodium citrate buffer in PBS) for 2 h at room temperature. To stain for neurites, explants were incubated with mouse anti-β Tubulin III (TUJ1) antibody (1:500, Novus Biologicals,

NB600-1018) overnight at 4°C followed by Alexa Fluor 594-conjugated secondary antibody (1:500, Jackson ImmunoResearch) for 2 h at room temperature. All antibodies were diluted in a staining buffer consisting of 0.5% Triton X-100, 0.1% Tween-20 and 5% BSA in PBS. Between changes of solution, explants were washed 3 times, 10 min each with PBS. After mounting onto Superfrost Plus Slides (VWR, 48311-703) with Fluoromount-G (SouthernBiotech, 0100-20), explants were imaged with a Leica fluorescence microscope (Leica Microsystems, DMi8). The neurite number and length of each retinal explants were quantified using the built-in software LAS X of the microscope (Leica Microsystems, Leica Application Suite X) by individuals blinded to the experimental groups.

**Optic nerve crush injury**

Mice were anesthetized by inhalation of 3-4% isoflurane for induction and 1-3% isoflurane for maintenance. Detailed surgical procedure of unilateral optic nerve crush (ONC) has been described previously[5,6]. In brief, a small incision was made in the temporal conjunctiva of the mouse eye, and the optic nerve was exposed and crushed with a Dumont #5 jeweler's forceps (FST) for about 5 sec, approximately 0.5 mm behind the eyeball. Proparacaine and antibiotic ointment were applied to the ocular surface before and after the crush, respectively. Buprenorphine SR or Ethiqa X were given subcutaneously as a postoperative analgesic.

**Immunohistochemistry of cryosections**

Mouse eye and brain were dissected out after transcardiac perfusion with 4% PFA in PBS. Tissues were post-fixed in 4% PFA overnight and then cryoprotected in 30% sucrose overnight at 4°C. For cryosections of the eye, cornea and lens were removed from the eye before being embedded in OCT compound (VWR, 25608-930) and frozen. The frozen tissue block was then sliced into 16 μm serial cross sections, collected on Superfrost Plus Slides and stored at -20°C until processed. Frozen sections were blocked with BSA (5%) and Triton X-100 (1%) in TBS for 1 h at room temperature, followed by incubation with the primary antibodies overnight at 4°C and then the proper secondary antibodies (1:500, Alexa Fluor 488, 594, 647 conjugated; Jackson ImmunoResearch) for 2 h at room temperature in the same blocking solution. Between changes of antibody incubation, all sections were washed 3 times, 5 min each. For staining of cholera toxin subunit B (CTB), after primary antibody, sections were incubated with biotin anti-goat (1:250, Vector Laboratories, BA-9500) for 2 h and Alexa Fluor 594-conjugated streptavidin (1:500, Thermo Scientific, S32356) for 1 h at room temperature. Primary antibodies used are goat anti-CTB (1:4000, List Biological Laboratories, 703), guinea pig anti-RBPMS (1:200,

PhosphoSolutions, 1830-RBPMS), and mouse anti-DNMT3a (1:100, Novus Biologicals, NB120-13888SS). Staining for anti-DNMT3a required 2N HCl treatment for 30 min at 37°C followed by neutralization with 0.1M Trish-HCl (pH 8.3) for 10 min at room temperature before the blocking.

For cryosections of the brain, OCT-embedded tissue block was cut into 40 μm serial cross sections, collected in cryoprotectant solution and stored at -20°C until processed. The floating brain sections were blocked with Background Buster (Newcomer Supply, NB306-50) for 30 min at room temperature followed by a previously published staining protocol with slight modification. Briefly, after 4-day primary incubation with goat anti-CTB (1:4000) at 4°C, floating sections were stained with biotin anti-goat for 2 h (1:200) and Alexa Fluor 594-conjugated streptavidin (1:1000) for 2 h at room temperature.

Immunostained samples were mounted with Fluoromount-G and imaged using Leica DMi8 fluorescence microscope and Leica SP8 confocal microscope (Leica Microsystems) with 20x and 40x lens, and Olympus FluoView FV3000 confocal laser scanning microscope (Olympus Life Science) with 4x lens. Tile scans of 3 – 4 consecutive retinal and longitudinal optic nerve sections per animal were imaged and used for RGC and axon quantification where data from the scans were averaged for individuals. Projection of Brain Z-scans was carried out using the ImageJ (1.53t) Fiji (2.13.1) with the 'Average intensity' projection option. Quantification of regenerated axons was adapted from protocols described previously[7]. In brief, within the microscope's built-in software LAS X, the fluorescence intensities of CTB-positive axons at different distances post the crush site were measured as the integrated density of the Region of Interest (ROI) subtracting the background. For quantification of RGC density in retinal sections, retinal sections containing the optic nerve head (thus crossing over the central and peripheral retinal regions) were used. The total number of RGCs in each retinal section was recorded and divided by the length of the entire retinal section. The quantifications were performed by individuals blinded to the experimental conditions.

**Optomotor response-based visual acuity test**

The optomotor reflex-based spatial frequency threshold test was performed as described previously to measure the visual acuity of mice[4]. A mouse was placed on a pedestal in the center of an area surrounded by four LCD screens (Acer 15-inch) that displayed black and white stripes in a grating pattern, which rotated clockwise or counter-clockwise. Each eye was tested separately based on the direction of the rotating stripes. Two observers watched the mouse's

tracking behavior, and a positive response was determined when the mouse head followed the grating movement. The rotation speed and contrast were kept constant. The width of the bars was varied to test how fine the mouse could see, and the corresponding bar width was calculated in term of cycle/degree where 0.4~0.5 cycle/degree reflects normal visual acuity in mouse. The responses were measured before and after treatment by individuals blinded to the group or treatment of the mouse. Mice with bleeding or inflammation after surgical procedures were excluded from the analysis. The exclusion criteria were established before the experiment.

**Light/dark preference test**

The light/dark preference test is based on the propensity of mice to prefer dark over bright environments[8]. A mouse was placed in a box with a light and a dark chamber connected by a small opening to allow free transitions between these two chambers. Mice that can see light show a preference for the dark chamber while blind mice would have no preference. No eyes were covered during baseline measurement while the contralateral eyelid was sutured to prevent the uninjured eye from seeing when tested after crush. Each mouse was kept in the box for 5 minutes and the time it spent in the dark chamber was calculated as a percentage of the total time in the box. In a preliminary study, we showed that mice with both eyes sutured exhibited no preference for the dark chamber as the blind mice, indication of effective blockade of light perception by suturing the eye as it was reported[9].

**Electroretinography and visual evoked potential**

Electroretinography of positive scotopic threshold response (pSTR) and visual evoked potential (VEP) were measured as described previously[4,10]. For pSTR recording, mice were dark adapted for 6 – 12 h before experiment started; while for VEP recording, mice were briefly adapted to dim red light (5 – 10 min) beforehand. Mice were anaesthetized with ketamine/xylazine (100 mg kg−1 and 20 mg kg−1). A drop of 1% tropicamide ophthalmic solution (Bausch & Lomb Inc., Tampa, FL, USA) was applied to dilate the pupils. Dim red light was on throughout the procedure and mice were kept on a built-in warming platform in the Ganzfield ColorDome (ColorDome LabCradle mouse ERG testing, Diagnosys LLC) to prevent hypothermia. Gold wire electrodes contacting both corneas were used to record pSTR with a reference and a ground needle electrode inserted subcutaneously between the eyes and at the base of the tail, respectively. Lights at intensities 6.57E-5 cd.s/m$^2$ and 1.7E-4 cd.s/m$^2$ were flashed in the dome to elicit pSTR per intensity. An average of 40 responses were recorded by the ERG system (Espion Electroretinography System, Diagnosys LLC) and the b-wave amplitude was measured

from the baseline to the positive peak. For VEP, electrode needles were placed subcutaneously at the snout, between the ears, and at the base of the tail. The contralateral eye was covered with a dark patch when recording the ipsilateral eye and vice versa. VEP was stimulated by 100 flashes at 3.0 cd.s/$m^2$ and the averaged response was recorded by the ERG system.

**Single-nuclei RNA sequencing**

Single-nuclei RNA sequencing was performed based on a previously described method[11]. Retinas from the ONC eyes were collected from 6 control and 6 *CKO*$^{Dnmt3a+/-}$ mice, respectively, at 2 days after injury (1 eye/mouse). To extract nuclei, frozen retinal tissues were homogenized in a Dounce homogenizer in 1 ml NP-40 lysis buffer and pelleted at 500 rcf for 5 min. The nuclei were stained for RBFOX3/NeuN (1:300, Sigma, #FCMAB317PE or #MAB377A5) and PTPRC/CD45 (1:300, BD Pharmingen, clone 30-F11) to enrich RGCs and immune cells, respectively. NeuN+ and CD45+ single nuclei were collected in separate tubes using a flow cytometer, and again pelleted at 500 rcf for 5 min. The nuclei were resuspended in 0.04% non-acetylated BSA/PBS solution, adjusted to a concentration of 1000 nuclei/µL, and loaded into a 10X Chromium Single Cell Chip (10X Genomics, Pleasanton, CA) with a targeted recovery of 8000 nuclei. As a result, we sequenced a total of 17,895 nuclei in the control group (Neun+, 9210; CD45+, 8685) and 16,683 nuclei in the *CKO*$^{Dnmt3a+/-}$ group (Neun+, 8235; CD45+, 8448). Single nuclei libraries were generated using the Chromium 3' V3.1 platform (10X Genomics, Pleasanton, CA) following the manufacturer's protocol, and sequenced on an Illumina NovaSeq at the Bauer Core Facility at Harvard University.

**Single-nuclei RNA-seq data analysis**

Data were processed in Cell ranger[12] to generate the output folder with barcodes, matrix and genes files. Those files were used to generate Seurat object using CreateSeuratObject() function in Seurat package[13,14]. We filtered data to remove doublets, low quality cells and empty droplets and performed filtering based on features/counts/mitochondrial genes/ribosomal genes following standard Seurat pipeline[15]. After data quality control and filtering, a total of 34,102 nuclei from both experimental groups were used for downstream analysis. Sequentially, data were normalized using the "NormalizeData" method, 2000 highly variable features were selected, data were centered, scaled, and clustered with Louvain algorithm[16]. UMAP was chosen as a non-linear dimensionality reduction approach[17].

We utilized DimPlot() and FeaturePlot() functions in Seurat as visualization methods for the data annotation. By obtaining the differentially expressed genes list with the function FindAllMarkers(only.pos = TRUE, min.pct = 0.25, log2FC.threshold = 0.25), we performed manual annotation for the dataset clusters (object$seurat_clusters) upon integrating the conditions (Control and *CKO*$^{Dnmt3a+/-}$). The integration was performed using the IntegrateData() function available in Seurat v4. We identified retinal ganglion cells (RGCs), immune cells, Müller glia, amacrine cells, horizontal cells, bipolar neurons, astrocytes, retinal pigment epithelium, rods, and cones, using expression of genes known to be selective markers for each cell class[18]. The immune cells population contained of microglia/macrophages (Klra17+, C1qc+, Cx3cr1+, Tmem119+), T helpers (H2-Ab1+, Cd74+), T cells (Grap2+, Itgb7+). As the total number of immune cells in the populations was small, we labeled them as 'Immune' for the downstream analysis. FindAllMarkers() function was used to identify the gene expression dynamics between the conditions on total RGC subset of the dataset.

We reclustered RGCs, normalized them using SCTransform method[19] and used previously identified type-specific markers for RGC types identification[20]. With the type markers list, we utilized AverageExpression() Seurat function to obtain the gene expression matrix and visualized it using DotPlot() function. Upon identification based on the gene expression, we annotated 35 clusters that contained 42 out of 45 known RGC types[20]. In detail, from those 42 types, we could reach the resolution of 21 types in 24 separate clusters (1:1), with the other 21 types represented in 11 clusters, each of which contained 2 – 4 RGC types (W3D1 | W3L1, M1a | M2, alpha OFF-T | alpha ON-T). The reason we could not reach the resolution of RGC types published by Tran et al[20] is likely due to the relatively small number of cells available for this analysis.

To visualize RGC type-specific marker gene expression, we generated a matrix of RGC Louvain clusters (object$seurat_clusters) with the expression values for the query gene of interest. We normalized the gene expression 'n' from 0 to 1 for every gene k independently per cluster c (formula 1) and generated the values of gene patterns expression p for the gene patterns m (Gene1+Gene2+, Gene1+Gene2+Gene3-, etc.) by summarizing the normalized gene expression values 'n' per cluster c (formula 2). Upon receiving the values per pattern showing the gene pattern expression p, those were normalized from 0 to 1 per pattern m independently for every cluster c. The resulting matrix of normalized gene expression patterns 'N' was visualized using ggplot2 geom_tile()[21].

Formula 1:

$$n_{k,c} = (x_{k,c} - \min k)(\max k - \min k)$$

Formula 2:

$$p_{m,c} = n_{m_1,c} \pm n_{m_2,c} \pm n_{m_y,c}$$

Formula 3:

$$N_{m,c} = (p_{m,c} - \min m)(\max m - \min m)$$

To unravel cell-cell interactions, we utilized CellChat package[22]. For that, we performed two parallel analyses between the conditions: 1) merged RGC clusters vs. every other cluster in the dataset (immune cells, Müller glia, amacrine cells, horizontal cells, bipolar neurons, astrocytes, retinal pigment epithelium, rods, and cones); 2) subset RGC and performed the same type of the analysis for RGC clusters.

The analysis included the CellChat approach to generate total incoming/outgoing signaling and chord diagrams between Control and *CKO*$^{Dnmt3a+/-}$ cells with additional settings. Those included type = "truncatedMean", trim = 0.1, raw.use = FALSE, population.size = TRUE for computeCommunProb() function. Upon generating the data, we merged data of horizontal cells, bipolar neurons, astrocytes, retinal pigment epithelium, rods, and cones and labeled those as ‘rest. For the results, we demonstrated outgoing signaling using pattern = ‘outgoing’ setting for the netAnalysis_signalingRole_heatmap() function and chord diagrams using netVisual_aggregate() function. We exported the computational probability to enable the communications comparisons between the cell types and conditions that were stored in the object as cellchat_object@netP$centr$pathway_name$outdeg and performed 0 to 1 normalization to visualize the data.

To perform GSEA pathway analysis, we utilized the escape package[23]. We loaded C5 pathways from Molecular Signatures Database[24,25] (‘GOBP_NEURON_DEATH’, 'GOBP_DENDRITE_EXTENSION', 'GOBP_OPTIC_NERVE_MORPHOGENESIS', 'GOBP_AXON_DEVELOPMENT', 'GOBP_REGULATION_OF_AXONOGENESIS', 'GOBP_RESPONSE_TO_AXON_INJURY',

‘GOBP_INFLAMMATORY_RESPONSE’, ’GOBP_INFLAMMASOME_COMPLEX_ASSEMBLY’, ‘GOBP_ACUTE_INFLAMMATORY_RESPONSE’, ‘GOBP_CYTOKINE_PRODUCTION_INVOLVED_IN_INFLAMMATORY_RESPONSE’, ‘GOBP_NEUROINFLAMMATORY_RESPONSE’) and performed ssGSEA enrichment[24]. ggplot2 and ggpubr packages[26] were used for the data visualization.

Then, we generalized the pathways used for GSEA analysis into three programs: neuronal injury, inflammation, and regeneration. The neuronal injury program included ‘GOBP_NEURON_DEATH’ and 'GOBP_RESPONSE_TO_AXON_INJURY' pathways. The inflammation program included ‘GOBP_INFLAMMATORY_RESPONSE’, ’GOBP_INFLAMMASOME_COMPLEX_ASSEMBLY’, ‘GOBP_ACUTE_INFLAMMATORY_RESPONSE’, ‘GOBP_CYTOKINE_PRODUCTION_INVOLVED_IN_INFLAMMATORY_RESPONSE’, and ‘GOBP_NEUROINFLAMMATORY_RESPONSE’ pathways. The regeneration program included 'GOBP_DENDRITE_EXTENSION', 'GOBP_OPTIC_NERVE_MORPHOGENESIS', 'GOBP_AXON_DEVELOPMENT', and 'GOBP_REGULATION_OF_AXONOGENESIS' pathways.

To normalize the contribution of the pathways to their corresponding programs from 0 to 1 (due to different average expressions and the amount of the pathways used), we generated the matrix of normalized pathway average expression ‘A’ for every pathway k per cluster c, using the pathway average expression ‘A’ data generated with GSEA analysis approach (formula 4).

Formula 4:

$$A_{k,c} = (a_{k,c} - \min k)(\max k - \min k)$$

Then, we quantified the pattern average expression ‘m’ for pathway mode y per cluster c as a summation of n pathways average expression A per cluster c with n = 5 for injury, n = 2 for inflammation, and n = 4 for regeneration program (formula 5).

Formula 5:

$$m_{y,c} = \sum_{i=k}^{n} A_{i,c} = A_{k,c} + A_{k_1,c} + A_{n,c}$$

Finally, we quantified the 0 to 1 normalized program average expression 'M' for pathway mode y per cluster c as a max/min normalization of program average expression m (formula 6).

Formula 6:

$$M_{y,c} = (m_{y,c} - \min y)(\max y - \min y)$$

The resulting matrix of RGC subtypes and programs was visualized using geom_point() and geom_line() functions of ggplot2 package with the programs separated using ~facet_wrap() function. We also performed the 3D visualization for neuronal injury/inflammation/regeneration patterns using plotly package (Extended Data HTML File), and 2D embeddings for injury/regeneration and inflammation/regeneration programs to demonstrate the distribution of RGC subtypes. For 2D and 3D embeddings, the values used are quantified as a difference of normalized program average expression M for pathway mode y per cluster c between *CKO*$^{Dnmt3a+/-}$ and Control conditions.

**Whole genome bisulfite-seq analysis**

DNA used for bisulfite sequencing were extracted from RGCs isolated from the injured eye at 2 days post-ONC. For each group, RGCs from 2 mice retinas were combined for DNA extraction (n = 2 mice/group, 1 eye/mouse). Bisulfite sequencing and data analysis was performed by Novogene. Basic statistics on the quality of the raw reads was processed by FastQC (fastqc_v0.11.5)[27]. The read sequences produced by the Illumina pipeline in FASTQ format were pre-processed through Trimmomatic (Trimmomatic-0.36) software[28] using the parameter (SLIDINGWINDOW:4:15; LEADING:3, TRAILING:3; ILLUMINACLIP: adapter.fa: 2: 30: 10; MINLEN:36). The remaining reads that passed all the filtering steps were counted as clean reads and all subsequent analyses were based on this. Finally, we used FastQC to perform basic statistics on the quality of the clean data reads. Bismark software (version 0.16.3)[29] was used to perform alignments of bisulfite-treated reads to a reference genome (-X 700 --dovetail). The reference genome was first transformed into bisulfite-converted version (C-to-T and G-to-A converted) and then indexed using bowtie2[30]. Sequence reads were also transformed into fully bisulfite-converted versions (C-to-T and G-to-A converted) before they are aligned to similarly converted versions of the genome in a directional manner. Sequence reads that produce a unique best alignment from the two alignment processes (original top and bottom strand) are then compared to the normal genomic sequence and the methylation state of all cytosine

positions in the read is inferred. The same reads that aligned to the same regions of genome were regarded as duplicated ones. The sequencing depth and coverage were summarized using deduplicated reads. The results of methylation extractor (bismark_methylation_extractor, --no_overlap) were transformed into bigWig format for visualization using IGV browser[31]. The sodium bisulfite non-conversion rate was calculated as the percentage of cytosine sequenced at cytosine reference positions in the lambda genome.

To identify the methylation site, we modeled the sum Mc of methylated counts as a binomial (Bin) random variable with methylation rate. To calculate the methylation level of the sequence, we divided the sequence into multiple bins, with bin size is 10kb. The sum of methylated and unmethylated read counts in each window were calculated. Calculated ML was further corrected with the bisulfite non-conversion rate according to previous studies[32].

Differentially methylated regions (DMRs) were identified using the DSS software[33-35]. The core of DSS is a new dispersion shrinkage method for estimating the dispersion parameter from Gamma-Poisson or Beta-Binomial distributions[36]. DSS possesses three characteristics to detect DMRs. First, spatial correlation. Proper use of the information from neighboring Cytosine sites can help improve estimation of methylation levels at each Cytosine site, and hence improve DMR detection. Second, the read depth of the Cytosine sites provides information on precision that can be exploited to improve statistical tests for DMR detection. Finally, without biological replicate, DSS combines data from nearby Cytosine sites and uses them as 'pseudo-replicates' to estimate biological variance at specific locations. According to the distribution of DMRs through the genome, we defined the genes related to DMRs as genes whose gene body region (from TSS to TES) or promoter region (upstream 2kb from the TSS) have an overlap with the DMRs. We quantified the rich factor as the number of DMR-related genes (input genes) divided by the number of pathway genes for each pathway, and the resulting parameters (rich factor, methylation type, and p-value) for the pathways selected from top-20 sorted by p-value (input genes ≥ 20 per pathway) were visualized using geom_bar() and geom_point() ggplot2 functions.

**Bulk RNA-seq data analysis**

RNA used for bulk RNA sequencing were extracted from RGCs isolated from the injured eye at 2 days post-ONC (n = 3 eyes/group, 1 eye/mouse). Raw data (raw reads) of .fastq format were first processed through in-house perl scripts by Novogene. In this step, clean data (clean reads) were obtained by removing reads containing adapter, ploy-N and low-quality reads from raw

data. At the same time, Q20, Q30 and GC content of the clean data were calculated. All the downstream analyses were based on clean data with high quality.

Reference genome and gene model annotation files were downloaded from the genome website directly. The index of the reference genome was built using Hisat2 v2.0.5 and paired-end clean reads were aligned to the reference genome using Hisat2 v2.0.5[37]. The mapped reads of each sample were assembled by StringTie (v1.3.3b)[38] in a reference-based approach.

The reads numbers mapped to each gene was counted by featureCounts v1.5.0-p3[39]. FPKM of each gene was calculated based on the length of the gene and reads count mapped to this gene. Differential expression analysis of 3 conditions/groups (3 biological replicates per condition) was performed using the DESeq2 R package (1.20.0)[40]. DESeq2 provides statistical routines for determining differential expression in digital gene expression data using a model based on the negative binomial distribution. The resulting P-values were adjusted using Benjamini and Hochberg's approach for controlling the false discovery rate. Genes with an adjusted P-value ≤ 0.05 found by DESeq2 were assigned as differentially expressed (DEGs).

The KEGG and GO pathway annotations of the DEGs were performed with ShinyGo[41] version 0.76 with the FDR cutoff = 0.05. The top 10 up or down-regulated pathways that are relevant to RGCs were visualized in dotplots (input genes ≥ 5 per pathway, sorted by fold enrichment). For GSEA pathway analysis of the DESeq2 output, we utilized clusterProfiler[42], msigdbr[43], and org.Mm.eg.db[44]. For the pathways, Hallmark category (category = "H")[45] was used, and upon filtering and sorting data based on log2FC values, we generated the table with GSEA() function. The top RGC-relevant pathways were visualized using ggplot2 package (setSize ≥ 5, sorted by Normalized enrichment score, NES).

The volcano plot was generated with the DESeq2 output using the Enhanced Volcano package[46]. The genes labeled on the plot are the result of two approaches: 1) the most significant genes appearing in DESeq2 output by log2FC and adjusted p-value; 2) genes appearing significant in the single nuclei RNA-seq data, pathways related to differentially methylated regions, and experimental data.

**Cell-cell interactions atlas generation**

Upon generating the CellChat objects, we exported the indegree and outdegree representing the incoming and outgoing signaling, respectively. Those were used to generate the matrix consisting of cell barcodes as row names, while pathways (incoming), pathways (outgoing), ligands – ligand-receptor pairs:pathways (outgoing), receptors – ligand-receptor pairs:pathways (incoming) were used as column names. The CellChat object exported values were used to fill in the matrix.
The following objects generated were formatted to follow the unified structure of the objects to be deposited to the Broad Institute's Single Cell Portal.

**Data Availability**

The raw and processed data of bisulfite, bulk, and single nuclei transcriptomic experiments generated in this study have been deposited in the GEO database under accession codes: GSE229033 (bulk), GSE229034 (bisulfite), GSE228627 (single-nuclei). The single nuclei data can be explored at the Broad Institute's Single Cell Portal: https://singlecell.broadinstitute.org/single_cell/study/SCP2321/. The cell-cell interactions can be explored at: https://singlecell.broadinstitute.org/single_cell/study/SCP2333/ for the Control, and https://singlecell.broadinstitute.org/single_cell/study/SCP2351/ for the $CKO^{Dnmt3a+/-}$. The toolbox used to perform the data analysis is described in **Supplementary Table 3**.

**Code Availability**

The code for reproducing the bioinformatical analysis is available on the following GitHub repository: https://github.com/mcrewcow/Lydia_ChenLab_RGC_pONC_retina.

**Intravitreal injection in mice**

Procedure for intravitreal injection was essentially described[6]. During intravitreal injection, a pulled microcapillary tube was inserted just behind the ora serrata in the mouse peripheral retina. The vitreous was then partially removed (about 2 µl) to enable the injection of 2 µl of solution into the vitreous chamber. For experiments using AAVs, mice were kept in housing for at least two weeks after the injection of AAV to ensure that the target genes were stably expressed. For tracing regenerating axons anterogradely, 2 µl of 2 µg/µl CTB (List Biological Laboratories, 104) was injected intravitreally 2-3 days before mice were sacrificed at various time points to assess the extent of nerve regeneration after ONC.

**Adeno-associated viruses (AAV) constructs and production**

AAV serotype 2/2 (AAV2) was used in all virus-mediated knockdown experiments. For Dnmt3a gene knockdown, vectors were generated in-house where an AAV.Scramble (scrambled control (5' - cctaaggttaagtcgccctcgctcgagcgagggcgacttaaccttagg – 3') and two AAV.shRNAs targeting Dnmt3a (#1: 5' - cgctccgctgaaggaatatttctcgagaaatattccttcagcggagcg – 3' and #2: 5' - ggcatccactgtgaatgataactcgagttatcattcacagtggatgcc – 3') were designed using the GPP Web Portal (Broad Institute). The shRNA sequences were synthesized as single-stranded oligonucleotides, annealed, and inserted into pAAV-U6-sgRNA-CMV-GFP (Addgene #85451) at SapI and SapI sites. AAV2 were produced as described using a triple transfection approached in HEK293T cells in 15 cm dishes with polyethylenimine and were harvested after 60 h incubation, purified by iodixanol gradient ultracentrifugation, and quantified by quantitative PCR (titers: >1 × $10^{12}$ genome copies per ml). AAV2/2.CASI.CRE.RBG (AAV.Cre) and AAV2/2.CASI.EGFP.RBG (AAV.GFP) (titers: >1.02 × $10^{12}$ GC/mL) were purchased from the Gene Transfer Vector Core at Schepens Eye Research Institute.


1 Vong, L. *et al.* Leptin action on GABAergic neurons prevents obesity and reduces inhibitory tone to POMC neurons. *Neuron* **71**, 142-154 (2011). https://doi.org:10.1016/j.neuron.2011.05.028

2 Feng, J. *et al.* Dnmt1 and Dnmt3a maintain DNA methylation and regulate synaptic function in adult forebrain neurons. *Nat Neurosci* **13**, 423-430 (2010). https://doi.org:10.1038/nn.2514

3 Huang, X., Wu, D. Y., Chen, G., Manji, H. & Chen, D. F. Support of retinal ganglion cell survival and axon regeneration by lithium through a Bcl-2-dependent mechanism. *Invest Ophthalmol Vis Sci* **44**, 347-354 (2003). https://doi.org:10.1167/iovs.02-0198

4 Tang, Y. *et al.* Therapeutic Targeting of Retinal Immune Microenvironment With CSF-1 Receptor Antibody Promotes Visual Function Recovery After Ischemic Optic Neuropathy. *Front Immunol* **11**, 585918 (2020). https://doi.org:10.3389/fimmu.2020.585918

5 Lu, Y. *et al.* Reprogramming to recover youthful epigenetic information and restore vision. *Nature* **588**, 124-129 (2020). https://doi.org:10.1038/s41586-020-2975-4

6 Cho, K. S. *et al.* Re-establishing the regenerative potential of central nervous system axons in postnatal mice. *J Cell Sci* **118**, 863-872 (2005). https://doi.org:10.1242/jcs.01658

7 Schaeffer, J., Delpech, C., Albert, F., Belin, S. & Nawabi, H. Adult Mouse Retina Explants: From ex vivo to in vivo Model of Central Nervous System Injuries. *Front Mol Neurosci* **13**, 599948 (2020). https://doi.org:10.3389/fnmol.2020.599948

8 Gaub, B. M. *et al.* Restoration of visual function by expression of a light-gated mammalian ion channel in retinal ganglion cells or ON-bipolar cells. *Proc Natl Acad Sci U S A* **111**, E5574-5583 (2014). https://doi.org:10.1073/pnas.1414162111

9 Lim, J. H. *et al.* Neural activity promotes long-distance, target-specific regeneration of adult retinal axons. *Nat Neurosci* **19**, 1073-1084 (2016). https://doi.org:10.1038/nn.4340

10 Ridder, W. H., 3rd & Nusinowitz, S. The visual evoked potential in the mouse--origins and response characteristics. *Vision Res* **46**, 902-913 (2006). https://doi.org:10.1016/j.visres.2005.09.006

11 Hahn, J. *et al.* Evolution of neuronal cell classes and types in the vertebrate retina. *bioRxiv* (2023). https://doi.org:10.1101/2023.04.07.536039

12 Zheng, G. X. *et al.* Massively parallel digital transcriptional profiling of single cells. *Nat Commun* **8**, 14049 (2017). https://doi.org:10.1038/ncomms14049

13 Butler, A., Hoffman, P., Smibert, P., Papalexi, E. & Satija, R. Integrating single-cell transcriptomic data across different conditions, technologies, and species. *Nat Biotechnol* **36**, 411-420 (2018). https://doi.org:10.1038/nbt.4096

14 Hao, Y. *et al.* Dictionary learning for integrative, multimodal and scalable single-cell analysis. *Nat Biotechnol* (2023). https://doi.org:10.1038/s41587-023-01767-y

15 Seurat - Guided Clustering Tutorial. *https://satijalab.org/seurat/articles/pbmc3k_tutorial.html*

16 Blondel, V. D., Guillaume, J.-L., Lambiotte, R. & Lefebvre, E. Fast unfolding of communities in large networks. *Journal of Statistical Mechanics: Theory and Experiment* **2008**, P10008 (2008). https://doi.org:10.1088/1742-5468/2008/10/P10008

17 Leland McInnes, J. H., James Melville. UMAP: Uniform Manifold Approximation and Projection for Dimension Reduction. *arXiv:1802.03426* (2020). https://doi.org:10.48550/arXiv.1802.03426

18 Yan, W. *et al.* Mouse Retinal Cell Atlas: Molecular Identification of over Sixty Amacrine Cell Types. *J Neurosci* **40**, 5177-5195 (2020). https://doi.org:10.1523/JNEUROSCI.0471-20.2020

19 Hafemeister, C. & Satija, R. Normalization and variance stabilization of single-cell RNA-seq data using regularized negative binomial regression. *Genome Biol* **20**, 296 (2019). https://doi.org:10.1186/s13059-019-1874-1

20 Tran, N. M. *et al.* Single-Cell Profiles of Retinal Ganglion Cells Differing in Resilience to Injury Reveal Neuroprotective Genes. *Neuron* **104**, 1039-1055 e1012 (2019). https://doi.org:10.1016/j.neuron.2019.11.006

21 H, W. ggplot2: Elegant Graphics for Data Analysis. *Springer-Verlag New York* **https://ggplot2.tidyverse.org** (2016).

22 Jin, S. *et al.* Inference and analysis of cell-cell communication using CellChat. *Nat Commun* **12**, 1088 (2021). https://doi.org:10.1038/s41467-021-21246-9

23 Borcherding, N. *et al.* Mapping the immune environment in clear cell renal carcinoma by single-cell genomics. *Commun Biol* **4**, 122 (2021). https://doi.org:10.1038/s42003-020-01625-6

24 Subramanian, A. *et al.* Gene set enrichment analysis: a knowledge-based approach for interpreting genome-wide expression profiles. *Proc Natl Acad Sci U S A* **102**, 15545-15550 (2005). https://doi.org:10.1073/pnas.0506580102

25 Mootha, V. K. *et al.* PGC-1alpha-responsive genes involved in oxidative phosphorylation are coordinately downregulated in human diabetes. *Nat Genet* **34**, 267-273 (2003). https://doi.org:10.1038/ng1180

26 Kassambara, A. ggpubr: 'ggplot2' Based Publication Ready Plots. *R package version 0.6.0* **https://rpkgs.datanovia.com/ggpubr/** (2023).

27 Andrews, S. A quality control tool for high throughput sequence data. *http://www.bioinformatics.babraham.ac.uk/projects/fastqc/* (2010).

28 Bolger, A. M., Lohse, M. & Usadel, B. Trimmomatic: a flexible trimmer for Illumina sequence data. *Bioinformatics* **30**, 2114-2120 (2014). https://doi.org:10.1093/bioinformatics/btu170

29 Krueger, F. & Andrews, S. R. Bismark: a flexible aligner and methylation caller for Bisulfite-Seq applications. *Bioinformatics* **27**, 1571-1572 (2011). https://doi.org:10.1093/bioinformatics/btr167

30 Langmead, B. & Salzberg, S. L. Fast gapped-read alignment with Bowtie 2. *Nat Methods* **9**, 357-359 (2012). https://doi.org:10.1038/nmeth.1923

31 Robinson, J. T. *et al.* Integrative genomics viewer. *Nat Biotechnol* **29**, 24-26 (2011). https://doi.org:10.1038/nbt.1754

32 Lister, R. *et al.* Global epigenomic reconfiguration during mammalian brain development. *Science* **341**, 1237905 (2013). https://doi.org:10.1126/science.1237905

33 Feng, H., Conneely, K. N. & Wu, H. A Bayesian hierarchical model to detect differentially methylated loci from single nucleotide resolution sequencing data. *Nucleic Acids Res* **42**, e69 (2014). https://doi.org:10.1093/nar/gku154

34 Wu, H. *et al.* Detection of differentially methylated regions from whole-genome bisulfite sequencing data without replicates. *Nucleic Acids Res* **43**, e141 (2015). https://doi.org:10.1093/nar/gkv715

35 Park, Y. & Wu, H. Differential methylation analysis for BS-seq data under general experimental design. *Bioinformatics* **32**, 1446-1453 (2016). https://doi.org:10.1093/bioinformatics/btw026

36 Aragon, J., David Eberly, and Shelly Eberly. Existence and uniqueness of the maximum likelihood estimator for the two-parameter negative binomial distribution. *Statistics and Probability Letters* **15 (5): 375–79** (1992). https://doi.org:10.1016/0167-7152(92)90157-Z

37 Kim, D., Paggi, J. M., Park, C., Bennett, C. & Salzberg, S. L. Graph-based genome alignment and genotyping with HISAT2 and HISAT-genotype. *Nat Biotechnol* **37**, 907-915 (2019). https://doi.org:10.1038/s41587-019-0201-4

38 Pertea, M. *et al.* StringTie enables improved reconstruction of a transcriptome from RNA-seq reads. *Nat Biotechnol* **33**, 290-295 (2015). https://doi.org:10.1038/nbt.3122

39 Liao, Y., Smyth, G. K. & Shi, W. featureCounts: an efficient general purpose program for assigning sequence reads to genomic features. *Bioinformatics* **30**, 923-930 (2014). https://doi.org:10.1093/bioinformatics/btt656

40 Love, M. I., Huber, W. & Anders, S. Moderated estimation of fold change and dispersion for RNA-seq data with DESeq2. *Genome Biol* **15**, 550 (2014). https://doi.org:10.1186/s13059-014-0550-8

41 Ge, S. X., Jung, D. & Yao, R. ShinyGO: a graphical gene-set enrichment tool for animals and plants. *Bioinformatics* **36**, 2628-2629 (2020). https://doi.org:10.1093/bioinformatics/btz931

42 Yu, G., Wang, L. G., Han, Y. & He, Q. Y. clusterProfiler: an R package for comparing biological themes among gene clusters. *OMICS* **16**, 284-287 (2012). https://doi.org:10.1089/omi.2011.0118

43 Dolgalev, I. msigdbr: MSigDB Gene Sets for Multiple Organisms in a Tidy Data Format. *R package version 7.5.1.9001* **https://igordot.github.io/msigdbr/** (2022).

44 Carlson, M. org.Mm.eg.db: Genome wide annotation for Mouse. *R package version 3.8.2.* (2019). https://doi.org:10.18129/B9.bioc.org.Mm.eg.db

45 Liberzon, A. *et al.* The Molecular Signatures Database (MSigDB) hallmark gene set collection. *Cell Syst* **1**, 417-425 (2015). https://doi.org:10.1016/j.cels.2015.12.004

46 Blighe K, R. S., Lewis M. EnhancedVolcano: Publication-ready volcano plots with enhanced colouring and labeling. *R package version 1.18.0* **https://github.com/kevinblighe/EnhancedVolcano** (2023).

**Fig.1**

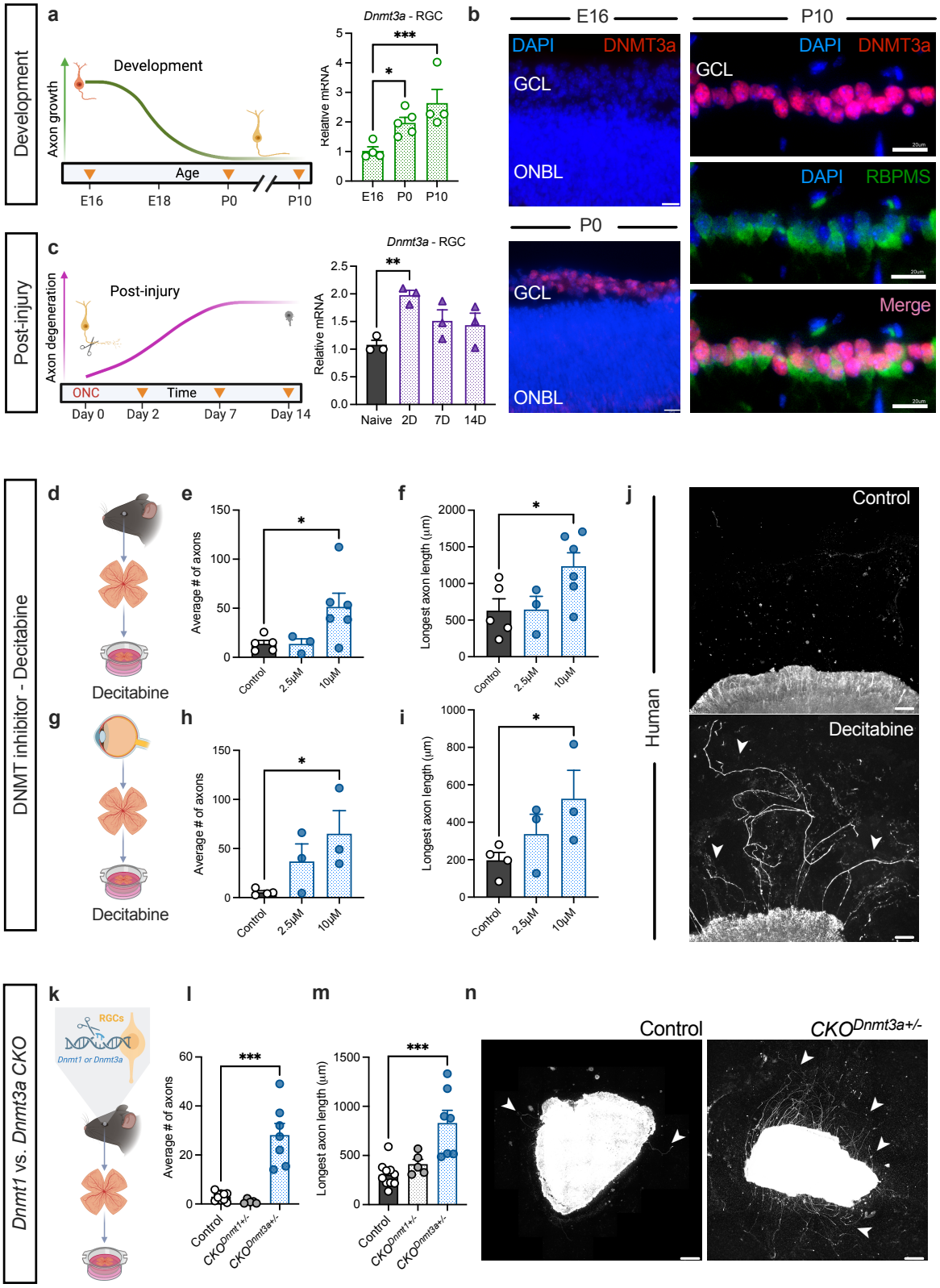
Development
a
Development
Axon growth
Age
E16
E18
P0
P10
Dnmt3a - RGC
Relative mRNA
E16
P0
P10
b
E16
P10
DAPI
DNMT3a
GCL
ONBL
DAPI
DNMT3a
GCL
DAPI
RBPMS
Merge
P0
GCL
ONBL
Post-injury
c
Post-injury
Axon degeneration
ONC
Time
Day 0
Day 2
Day 7
Day 14
Dnmt3a - RGC
Relative mRNA
Naive
2D
7D
14D
DNMT inhibitor - Decitabine
d
Decitabine
e
Average # of axons
Control
2.5μM
10μM
f
Longest axon length (μm)
g
Decitabine
h
Average # of axons
i
Longest axon length (μm)
j
Human
Control
Decitabine
Dnmt1 vs. Dnmt3a CKO
k
RGCs
Dnmt1 or Dnmt3a
l
Average # of axons
Control
CKODnmt1+/-
CKODnmt3a+/-
m
Longest axon length (μm)
n
Control
CKODnmt3a+/-

**Fig. 1. *Dnmt3a* deficiency enabled robust axonal outgrowth in retinal explants of mice and human.** **a**, Schematic of RGC axon growth timeline during development (left) and qPCR quantification of *Dnmt3a* expression in purified RGCs (right) (n = 4 – 5 mice/group); note the inverse correlation of *Dnmt3a* expression and RGC axon growth capacity from E16 to P10. **b**, Representative images of retinal sections from mice aged E16, P0, and P10 that were immunolabeled for DNMT3a (red) and an RGC marker RBPMS (green) and counter-stained with DAPI (blue). DNMT3a signal was first detected in the ganglion cell layer (GCL) at P0 and became intense and colocalized with RBPMS in P10 retinas. Scale bar: 20 μm. **c**, Schematic of axon degeneration timeline (left) and qPCR quantification of *Dnmt3a* expression in purified RGCs (right) from naïve and post-ONC mice (n = 3 mice/group). **d-i**, Schematics of experiments presented in **e** and **f** (**d**) or **h-j** (**g**), and quantification of axon number (**e**, **h**) and longest axon length (**f**, **i**) in retinal explant cultures derived from adult mice (**e**, **f**) and post-mortem human eyes (**h**, **i**) that were treated with various doses of a pan DNMT inhibitor decitabine (n = 3 – 6 mice/group). **j**. Representative images of cultured human retinal explants treated with vehicle (control) or decitabine (bottom) and immunolabeled for βIII-tubulin to reveal growing axons. Scale bar: 100 μm. **k-m**, Schematic of experiments presented in **l-n** (**k**) and quantification (**l**, **m**) of axon number (**l**) and longest axon length (**m**) in cultured retinal explants taken from mutant and littermate control (*Cre* and *fl/+*) mice (n ≥ 5 mice/group). **n**, Representative images of cultured retinal explants taken from littermate control (left) and $CKO^{Dnmt3a}$ (right) mice that were immunolabeled for β-III tubulin. Scale bar: 400 μm. ONBL, outer neuroblastic layer. White arrows denote neurites (*$P < 0.05$, **$P < 0.01$, ***$P < 0.001$, one-way ANOVA; mean ± s.e.m.)

**Fig. 2**

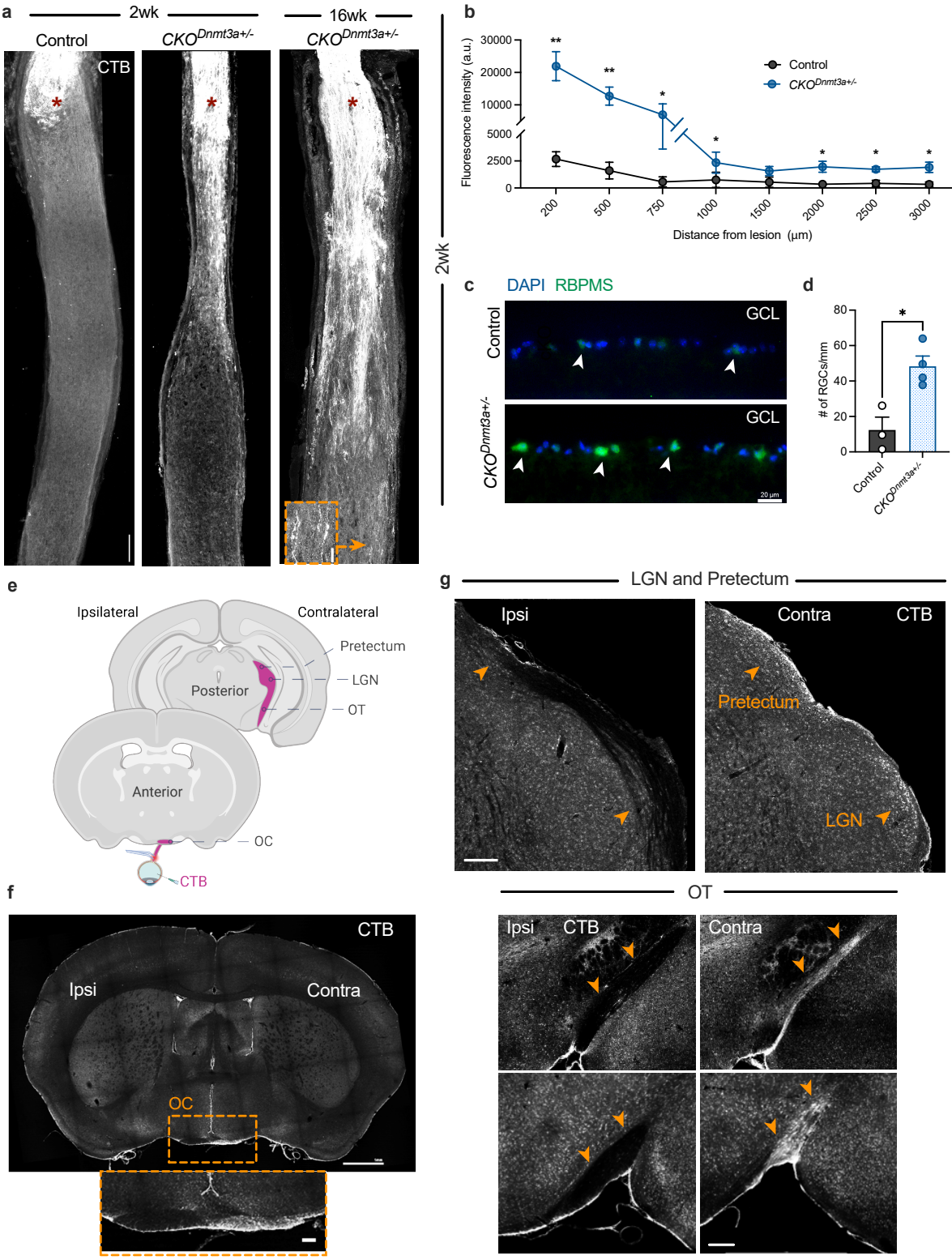
a
2wk
16wk
Control
CKO Dnmt3a+/-
CKO Dnmt3a+/-
CTB
b
Fluorescence intensity (a.u.)
30000
20000
10000
5000
2500
0
Control
CKO Dnmt3a+/-
200
500
750
1000
1500
2000
2500
3000
Distance from lesion (μm)
2wk
c
DAPI RBPMS
Control
CKO Dnmt3a+/-
GCL
GCL
20 μm
d
# of RGCs/mm
80
60
40
20
0
Control
CKO Dnmt3a+/-
e
Ipsilateral
Contralateral
Pretectum
LGN
OT
Posterior
Anterior
OC
CTB
f
CTB
Ipsi
Contra
OC
g
LGN and Pretectum
Ipsi
Contra
CTB
Pretectum
LGN
OT
Ipsi
CTB
Contra

**Fig. 2. Full-length optic nerve regeneration and target reinnervation after ONC in *CKO*$^{Dnmt3+/-}$ mice. a**, Representative images of longitudinal optic nerve sections showing CTB labeled axons in control and *CKO*$^{Dnmt3a+/-}$ mice at 2- or 16-week post-ONC. Each image is an overlay of 3 consecutive nerve sections. Asterisk indicates the crush site. Scale bar: 100 µm; inset: 20 µm. **b**, Quantification of axon regeneration by CTB-labeled fluorescent intensity at various distances distal to the crush site at 2 weeks post-ONC (n = 5 mice/group). **c**, Representative images of retinal sections taken from control and *CKO*$^{Dnmt3a+/-}$ mice at 2 weeks post-ONC that were immunolabeled with anti-RBPMS antibody (green) and counter-stained with DAPI (blue). GCL, ganglion cell layer; scale bar: 20 µm. **d**, Quantification of RGC survival by counting RBPMS+ cells in retinal sections at 2 weeks post-ONC. White arrows denote RBPMS+ cells (n = 3 – 4 mice/group). **e**, Schematic of the path of regenerating axons highlighted in purple color, showing their entrance primarily into the contralateral optic chiasm (OC) and optic tract (OT) to innervate the lateral geniculate nucleus (LGN) and Pretectal area. **f-g**, Representative images of brain sections from *CKO*$^{Dnmt3a+/-}$ mice at 16 weeks post-crush showing CTB-labeled axons innervating the contralateral (Contra) OC (**f,** scale bar: 1 mm; inset: 100 µm), OT (**g,** scale bar: 200 µm), LGN and pretectum (**g**, scale bar: 200 µm), but not seen in the ipsilateral side (Ipsi). Arrows denote the path of OT, LGN and pretectal areas in Contra and Ipsi brain sections. Insets are circled by orange dash lines. *$P < 0.05$, **$P < 0.01$; for **b**, multiple unpaired t-tests; for **d**, unpaired t-test; mean ± s.e.m.

**Fig. 3**

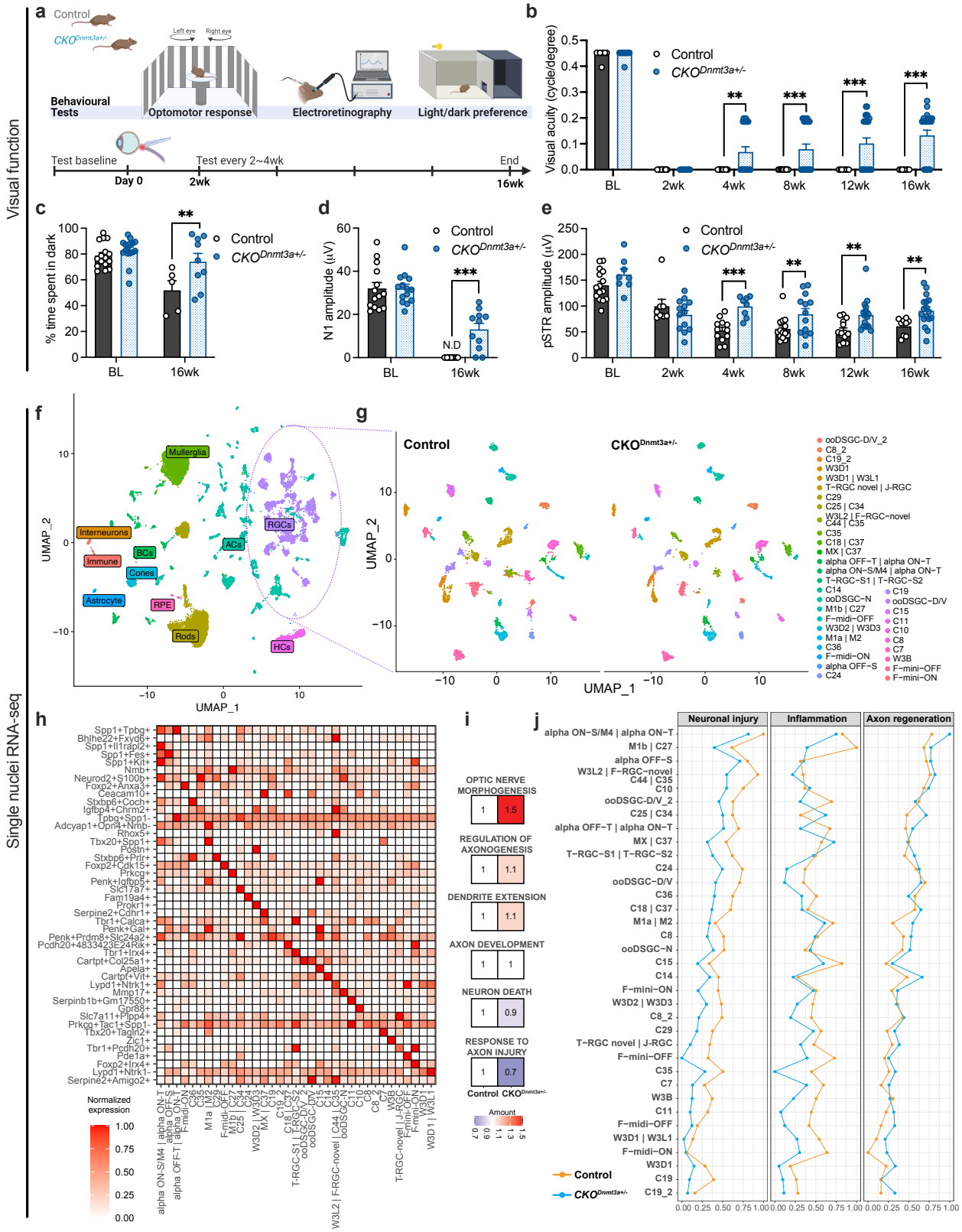
Visual function
Single nuclei RNA-seq
a
Control
CKODnmt3a+/-
Left eye
Right eye
Behavioural Tests
Optomotor response
Electroretinography
Light/dark preference
Test baseline
Day 0
Test every 2~4wk
2wk
End
16wk
b
Visual acuity (cycle/degree)
Control
CKODnmt3a+/-
BL
2wk
4wk
8wk
12wk
16wk
c
% time spent in dark
d
N1 amplitude (μV)
N.D
e
pSTR amplitude (μV)
f
Mullerglia
Interneurons
Immune
BCs
Cones
Astrocyte
RPE
Rods
ACs
RGCs
HCs
UMAP_1
UMAP_2
g
Control
CKODnmt3a+/-
h
Normalized expression
i
OPTIC NERVE MORPHOGENESIS
REGULATION OF AXONOGENESIS
DENDRITE EXTENSION
AXON DEVELOPMENT
NEURON DEATH
RESPONSE TO AXON INJURY
Control
CKODnmt3a+/-
Amount
j
Neuronal injury
Inflammation
Axon regeneration
Control
CKODnmt3a+/-

**Fig. 3. Visual function recovery following ONC in *Dnmt3a* deficient mice. a**, Schematic of the experiments presented in **b**-**e**. **b**, Quantification of visual acuity assessed by OMR in $CKO^{Dnmt3a+/-}$ and littermate control mice before (baseline, BL) and at 2 – 16 weeks (wk) after ONC (n ≥ 8 mice/group). **c**, Light perception assessed by the light/dark preference tests in $CKO^{Dnmt3a+/-}$ and littermate control mice before (BL) and at 16 weeks post-ONC; the assay measured the percentage of time spent in the dark chamber (n ≥ 5 mice/group). **d**, VEP N1 wave amplitudes in $CKO^{Dnmt3a+/-}$ and littermate control mice assessed before (BL) and at 16 weeks post-ONC (n ≥ 11 mice/group). **e**, RGC function measured by pSTR amplitudes in $CKO^{Dnmt3a+/-}$ and littermate control mice before (BL) and at 2 – 16 weeks after ONC (n ≥ 8 mice/group) (*$P < 0.05$, **$P < 0.01$, ***$P < 0.001$, multiple unpaired t-tests; mean ± s.e.m.). **f**, **g**, Dimplots showing detection of retinal cell (**f**) and RGC types (**g**) in the $CKO^{Dnmt3a+/-}$ and littermate control retinas (n = 6 retinas from 6 mice/group) at 2 days after ONC by single nuclei RNA-seq (snRNA-seq). **h**, Heatmap showing markers unique for each RGC cluster. X-axis indicates the RGC types (cluster annotation), and Y-axis displays the markers used for RGC type identification. **i**, Single-sample gene set enrichment analysis (ssGSEA) of DEGs from snRNA-seq datasets indicating increased strengths (normalized to controls) in optic nerve morphogenesis, axon genesis, and dendritic extension pathways and decreased strengths in neuronal death and response to axon injury pathways in $CKO^{Dnmt3a+/-}$ RGCs compared to controls. **j**, Combined GSEA scores in pathways related to neural injury, inflammation, and nerve regeneration among $CKO^{Dnmt3a+/-}$ (blue dotted line) and control (orange dotted line) RGC types. Normalization of the normalized enrichment scores (NES) was carried out using formulas 4 – 6 described in the Methods. The data revealed across-the-board downregulation of the neuronal injury and inflammation pathways but upregulation of nerve regeneration gene network strength in $CKO^{Dnmt3a+/-}$ RGCs compared to controls. N.D = not detected.

**Fig. 4**

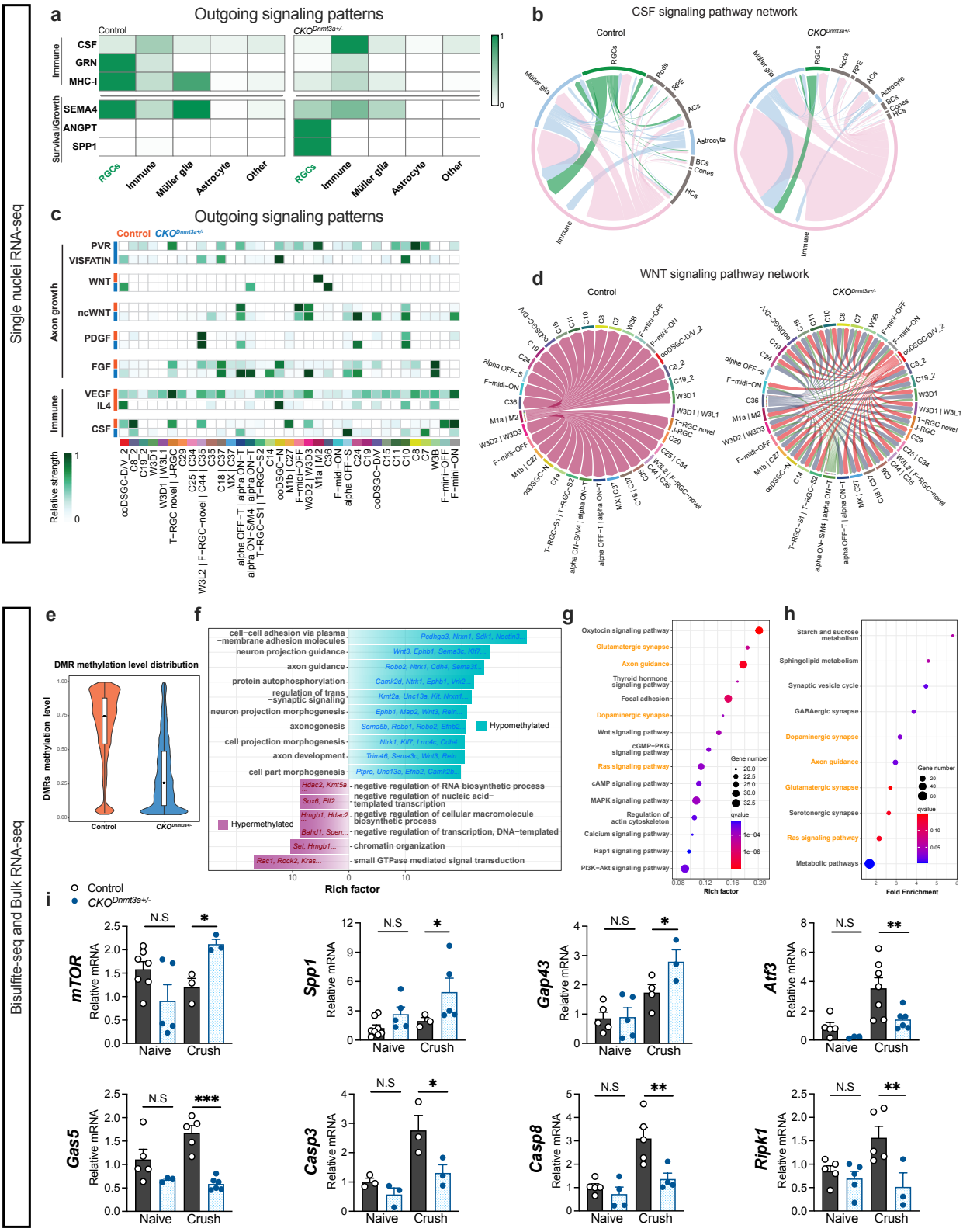
Single nuclei RNA-seq
Bisulfite-seq and Bulk RNA-seq
a
Outgoing signaling patterns
Control
CKODnmt3a+/-
Immune
CSF
GRN
MHC-I
Survival/Growth
SEMA4
ANGPT
SPP1
RGCs
Immune
Müller glia
Astrocyte
Other
b
CSF signaling pathway network
Control
CKODnmt3a+/-
RGCs
Rods
RPE
ACs
Astrocyte
BCs
Cones
HCs
Müller glia
Immune
c
Outgoing signaling patterns
Control CKODnmt3a+/-
Axon growth
PVR
VISFATIN
WNT
ncWNT
PDGF
FGF
Immune
VEGF
IL4
CSF
Relative strength
d
WNT signaling pathway network
Control
CKODnmt3a+/-
e
DMR methylation level distribution
DMRs methylation level
Control
CKODnmt3a+/-
f
cell−cell adhesion via plasma −membrane adhesion molecules
neuron projection guidance
axon guidance
protein autophosphorylation
regulation of trans −synaptic signaling
neuron projection morphogenesis
axonogenesis
cell projection morphogenesis
axon development
cell part morphogenesis
Hypomethylated
Hypermethylated
negative regulation of RNA biosynthetic process
negative regulation of nucleic acid−templated transcription
negative regulation of cellular macromolecule biosynthetic process
negative regulation of transcription, DNA−templated
chromatin organization
small GTPase mediated signal transduction
Rich factor
g
Oxytocin signaling pathway
Glutamatergic synapse
Axon guidance
Thyroid hormone signaling pathway
Focal adhesion
Dopaminergic synapse
Wnt signaling pathway
cGMP−PKG signaling pathway
Ras signaling pathway
cAMP signaling pathway
MAPK signaling pathway
Regulation of actin cytoskeleton
Calcium signaling pathway
Rap1 signaling pathway
PI3K−Akt signaling pathway
Gene number
qvalue
Rich factor
h
Starch and sucrose metabolism
Sphingolipid metabolism
Synaptic vesicle cycle
GABAergic synapse
Dopaminergic synapse
Axon guidance
Glutamatergic synapse
Serotonergic synapse
Ras signaling pathway
Metabolic pathways
Gene number
qvalue
Fold Enrichment
i
Control
CKODnmt3a+/-
mTOR
Spp1
Gap43
Atf3
Gas5
Casp3
Casp8
Ripk1
Relative mRNA
N.S
Naive
Crush

**Fig. 4. Activation of diverse axon regeneration pathways by *Dnmt3a* deficiency unveiled by multi-omics sequencing data. a**, Heatmap of cellular outgoing signals in the retina of $CKO^{Dnmt3a+/-}$ and control mice, predicted by the CellChat output analyses and selected from those showing drastic changes in $CKO^{Dnmt3a+/-}$ and control RGCs: note the downregulation of CSF, GRN, MHC-I and SEMA4 outgoing signals and upregulation of ANGPT and SPP1 outgoing signals in $CKO^{Dnmt3a+/-}$ RGCs. X-axis denotes cell populations: RGC, immune, Müller glia, amacrine, and others (including horizontal cells, bipolar neurons, astrocytes, retinal pigment epithelial cells, rods, and cones). Y-axis denotes signaling pathways (receptor-ligand pairs). **b**, Chord diagrams representing the intercellular CSF signaling among retinal cell types. The outgoing signal of RGCs was highlighted in green, while the outgoing signals from all other cell types were colored in gray or light pink to simplify the presentation. Arrows indicate the directions of the signals, and the arrow's width represents the relative signal strength. **c**, Heatmaps of outgoing signals sent among RGC types in control and $CKO^{Dnmt3a+/-}$ mice. Note that $CKO^{Dnmt3a+/-}$ RGCs displayed exclusive transmission of PVR and VISFATIN signals that were absent in control RGCs, while VEGF and IL-4 outgoing signals were observed solely among control RGC types. **d**, Chord diagrams showing intercellular WNT signaling among RGC types in control and $CKO^{Dnmt3a+/-}$ mice. **e**, Reduced DNA methylation at the differentially methylated regions (DMR) in $CKO^{Dnmt3a+/-}$ RGCs compared to controls as assessed by whole-genome bisulfite-seq (n = 2 mice/group). **f**, GO analysis of hyper- and hypo-methylated pathways and related genes. **g**, KEGG pathway enrichment of DMR-related gene pathways, selected from TOP-20. **h**, KEGG pathway analysis based on the upregulated DEGs from bulk RNA-seq transcriptome profiling of $CKO^{Dnmt3a+/-}$ and control RGCs (n = 3 mice/group). Note that the DMR-pathways identified in **g** and the upregulated signaling events in **h** are highly correlated – the common pathways found in both are highlighted in orange. **i**, qPCR quantification of selective genes reported to mediate axon regeneration, neural injury and inflammation in $CKO^{Dnmt3a+/-}$ and control RGCs isolated from naïve mice or mice at 2 days after ONC ($n \geq 3$ mice/group; $^{*}P < 0.05$, $^{**}P < 0.01$, $^{***}P < 0.001$, one-way ANOVA; mean ± s.e.m.).

**Fig. 5**

AAV.Scramble vs. AAV.shRNA in C57BL/6 mice

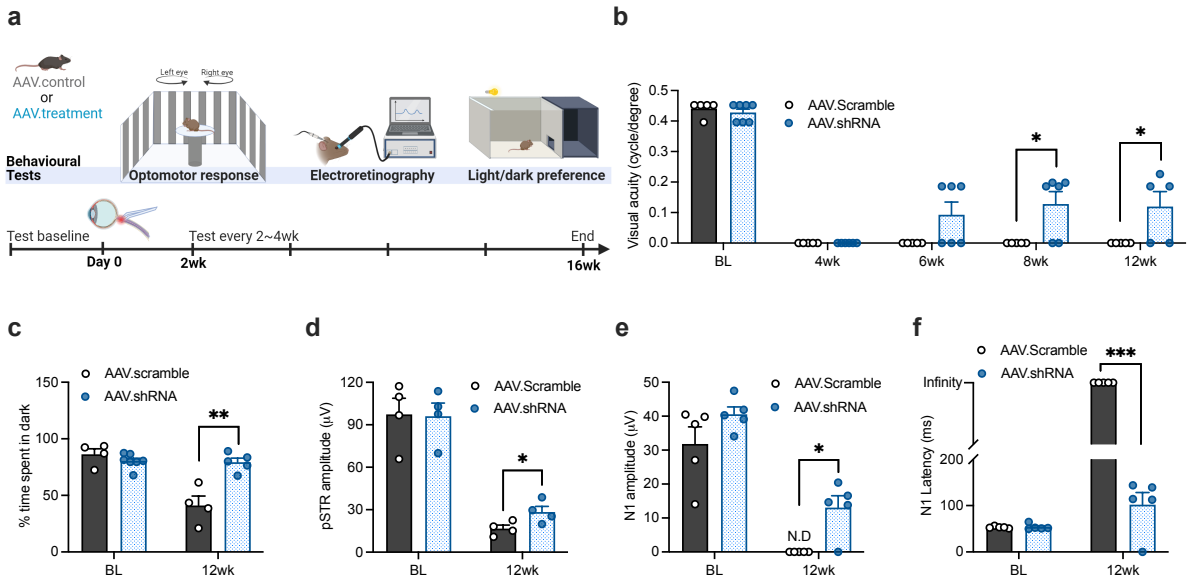


AAV.GFP vs. AAV.Cre in *Dnmt3a*$^{fl/+}$ mice

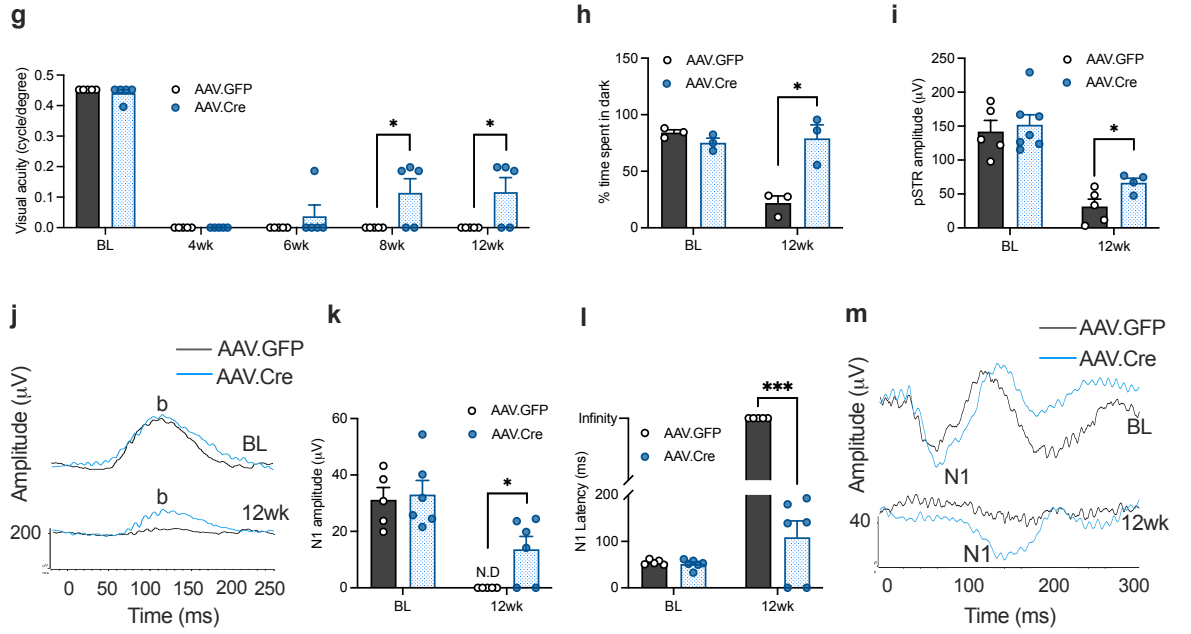

**Fig. 5. Restoration of vision following ONC in adult mice by therapeutic *Dnmt3a* knockdown.** **a**, Schematic of the experiments presented in **b-m**. **b**, Assessment of visual acuity by OMR assay in adult wildtype mice before (BL) and at 4 – 12 weeks after ONC; mice received intravitreal injection immediately after ONC of either control *AAV.scramble* or treatment *AAV.shRNA* that specifically targeted *Dnmt3a*. **c**, Percentage of times spent in the dark chamber by mice in the light/dark preference test. **d**, pSTR amplitudes. **e**, **f**, VEP N1 amplitude (**e**) and latency (**f**). **g**, Assessment of visual acuity by OMR assay in adult *Dnmt3a*$^{fl/+}$ mice before and at 4 – 12 weeks after ONC; mice received intravitreal injection immediately after ONC of either control *AAV.GFP* or treatment *AAV.Cre*. **h**, Percentage of time spent in the dark chamber by mice in the light/dark preference test. **i**, pSTR amplitude. **j**, Representative pSTR wave forms of (**i**). **k**, **l**, VEP N1 amplitude (**k**) and latency (**l**). **m**, Representative VEP waveforms of (**k**, **l**). ($n \geq 3$ mice/group; $^{*}P < 0.05$, $^{**}P < 0.01$, $^{***}P < 0.001$, multiple unpaired t-tests; mean ± s.e.m.).